# Simulation of a search for the Standard Model Higgs boson in the $H \to \gamma\gamma$ channel at LHC/ATLAS

*Unni I. Fuskeland*
University of Oslo
June 2002

Thesis presented for the Cand. Scient. degree
in Experimental Particle Physics

# Abstract

The channel $H \rightarrow \gamma\gamma$ is the most promising in which to discover a light Higgs boson with ATLAS at LHC. The ATLAS detector is one of the four experiments at the Large Hadron Collider at CERN and will, according to current planning, become operational in 2007. This thesis describes an analysis of the channel done with fast simulation of the signal and background processes in the mass range 120 - 150 GeV. The significance of the signal is calculated with the standard counting experiment technique and also with a more advanced statistical procedure. The concept of splitting the events into two channels where the signal resolution is different is also introduced.

# Acknowledgements

First of all, I would like to thank my supervisor Lars Bugge for giving me the idea of doing this interesting and challenging work, and for his support during this last $1\frac{1}{2}$ years. Thanks also goes to Alexander Read for help along the way regarding statistical problems, to Nils Lid Hjort for assistance with the development of the statistical methods, and to Børge Kile Gjelsten for valuable comments/opinions on the analysis. The whole experimental particle physics group here in Oslo have inspired and helped me, and they have made me feel included from the moment I came as a master student. Finally, I wish to thank Anette L. Borg and Bjørn H. Samset for morale support and for reading through some of the manuscript.

# Contents

**1 Introduction 3**

**2 The ATLAS detector 5**
- 2.1 CERN . . . . . 5
- 2.2 The Large Hadron Collider . . . . . 5
- 2.3 The ATLAS detector . . . . . 7
  - 2.3.1 Inner Detector . . . . . 9
  - 2.3.2 Calorimeters . . . . . 10
  - 2.3.3 Muon spectrometer . . . . . 11
  - 2.3.4 Magnet system . . . . . 12
  - 2.3.5 Trigger and data-acquisition system . . . . . 13

**3 Theory 15**
- 3.1 The Standard Model . . . . . 15
- 3.2 The Higgs mechanism . . . . . 16

**4 Software 21**
- 4.1 Simulation software; PYTHIA and ATLFAST . . . . . 21
- 4.2 Parallel computing . . . . . 21
- 4.3 Data analysis with PAW . . . . . 22

**5 Statistical methods 23**
- 5.1 The significance . . . . . 23
  - 5.1.1 The counting method . . . . . 23
  - 5.1.2 The chi-square method . . . . . 24
- 5.2 The significance with two channels . . . . . 25
  - 5.2.1 The counting method . . . . . 25
  - 5.2.2 The chi-square method . . . . . 26
- 5.3 The Higgs mass and its uncertainty with two channels . . . . . 26
- 5.4 ALRMC . . . . . 26

**6 The analysis 29**
- 6.1 The heritage from LEP . . . . . 29
- 6.2 Higgs search at LHC . . . . . 29
- 6.3 $H \to \gamma\gamma$ . . . . . 31
- 6.4 Background . . . . . 32

6.4.1 Irreducible; Born and box reactions . . . . . . . . . . . . . . . . . . 32
6.4.2 Irreducible; Bremsstrahlung reactions . . . . . . . . . . . . . . . . . 33
6.4.3 Reducible . . . . . . . . . . . . . . . . . . . . . . . . . . . . . . . 33
6.5 EM Calorimeter performance - Photon conversions . . . . . . . . . . . . 34
6.6 Radions . . . . . . . . . . . . . . . . . . . . . . . . . . . . . . . . . . . 35

**7 Results** **37**

7.1 Cuts . . . . . . . . . . . . . . . . . . . . . . . . . . . . . . . . . . . . . 37
7.2 Signal reconstruction . . . . . . . . . . . . . . . . . . . . . . . . . . . . 37
7.3 Background reconstruction . . . . . . . . . . . . . . . . . . . . . . . . . 40
7.3.1 Born and box . . . . . . . . . . . . . . . . . . . . . . . . . . . . . . 40
7.3.2 Bremsstrahlung . . . . . . . . . . . . . . . . . . . . . . . . . . . . . 40
7.3.3 Reducible . . . . . . . . . . . . . . . . . . . . . . . . . . . . . . . . 43
7.3.4 Discussion . . . . . . . . . . . . . . . . . . . . . . . . . . . . . . . . 43
7.4 Statistical treatment of the data . . . . . . . . . . . . . . . . . . . . . . 44
7.4.1 Significance found by using counting experiments . . . . . . . . . 47
7.4.2 Significance found by using the $\chi^2$ method . . . . . . . . . . . . . 48
7.4.3 Discussion . . . . . . . . . . . . . . . . . . . . . . . . . . . . . . . . 48
7.5 Reconstructed Higgs mass . . . . . . . . . . . . . . . . . . . . . . . . . 52

**8 Conclusion and Outlook** **53**

**A Simulation parameters** **55**

**B Significances for the three runs** **57**

**Bibliography** **61**

# Chapter 1

# Introduction

The existence of the Higgs particle was first brought up by a Scottish physicist in the 1960s [1]. The motivation was an open question in particle physics; how the particles get their masses. There is a clever solution to this problem, a solution first proposed by Peter Higgs. He proposed that the whole of space is permeated by a field, the Higgs field. As particles move through space they travel through this field, and if they interact with it, they acquire what appears to be mass. The larger the interaction of the particles with the field, the more massive they are. We know from quantum theory that fields have particles associated with them, like for instance the photon and the electromagnetic field. So we would assume that there is a particle associated with the Higgs field, and that is the Higgs boson. Finding the Higgs boson is thus the key of discovering whether the Higgs field does exist, and whether our best hypothesis for the origin of mass is indeed correct. Unfortunately, the electroweak theory does not predict the mass of the Higgs boson itself.

The first step toward finding the Higgs boson was the designing of LEP, an electron-positron collider at CERN. It was operational from 1989 to November 2000, but did not give evidence for the existence of the Higgs boson. During the last month of running, scientists at LEP announced that they had observed several unusual events which could have been the signature of the Higgs boson. CERN decided they would have another month of running. After that period, with conclusive evidence still lacking, dismantling started and the building of the next CERN collider, the LHC, proceeded. Before the Large Hadron Collider will be operational, Fermilab just outside Chicago will have a chance to observe the Higgs boson.

My project for this master thesis is to investigate a promising channel for observing a light Higgs boson, $H \rightarrow \gamma\gamma$. It is based on the analysis done for the ATLAS Technical Design Report (TDR) [2]. The first phase of the project is trying to reproduce the signal and background, however, to be able to finish in the prescribed time of a master project, I will only use fast simulation. That means I am not able to simulate the QCD background and not deal with generated converted photons, since that requires full simulation. In the other part of my thesis, I will calculate significances both by counting and by a more refined statistical method involving histogram chi-squares. I will also investigate a new technique; splitting the data into two channels. The idea is that this would increase the significance when the two signal resolutions are different.

The thesis is divided into eight chapters. Chapters 2 and 3 are the theoretical foundation, where the highlights are the ATLAS detector and the Higgs mechanism. The tools and methods are described in the next two chapters, while chapter 6 presents the important aspects in the analysis. Then there is a chapter presenting the results and at the end, conclusion and outlook. There are two appendixes, the first one describes some parameters used for the simulation and the second lists the significances for three sets of data.

# Chapter 2

# The ATLAS detector

## 2.1 CERN

CERN [3] is the European Organisation for Nuclear Research and is situated on the border between France and Switzerland, just outside Geneva. (Originally an abbreviation for Conseil Europèen pour la Recherche Nuclèaire.) It is one of the world's largest particle physics centres and has become a shining example of international collaboration. It was founded in 1954, and from the original 12 signatories of the CERN convention, membership has grown to the present 20 Member States. CERN employs almost 3000 people and in addition, some 6500 scientists come to CERN for their research, representing 500 universities and over 80 nationalities. Besides being a research laboratory, CERN also plays an important role in advanced technical education.

The biggest and most expensive project at CERN these days is the preparation of the Large Hadron Collider, the LHC.

## 2.2 The Large Hadron Collider

The Large Hadron Collider is presently under construction and will hopefully start the first run in 2007. The previous large accelerator at CERN, LEP, was shut down in November 2000, and dismantling started. LHC will use the old LEP tunnel which has a diameter of 8.6 km, measures 27 km in circumference and is contained in a tunnel 100 metres underground. In figure 2.1 you can see the whereabouts of the tunnel situated at the border between France and Switzerland. The smaller ring on the picture is the proton injector (SPS) while the triangular area in front of the small ring is the main CERN area. While LEP was an electron-positron collider, LHC will be colliding protons, and the energy available will reach the TeV range ($\sqrt{s} = 14$ TeV), about ten times higher than at LEP.

The luminosity in the LHC will reach $L = 10^{34}$ cm$^{-2}$s$^{-1}$ after three years of running (this is the *high luminosity* phase, while the first three years will have *low luminosity*,

Figure 2.1: The location of the LHC tunnel.

$10^{33}$ cm$^{-2}$s$^{-1}$). This will be achieved by filling each of the two rings[1] with 2835 bunches of $10^{11}$ particles each. The resulting large beam current is a particular challenge in a machine made of super-conducting magnets operating at cryogenic temperatures. The beams will be stored at high energy for about ten hours. During this time the particles make four hundred million revolutions. More details about the machine can be found in [5].

When designing the machine, it is very important to make it as flexible as possible while minimising the cost (money is always an issue). It may come in handy to be able to adapt to other situations, who knows what the next generation of colliders will need. As an example, the CERN SPS accelerator was first upgraded from a fixed target proton machine into a proton-antiproton collider, then a heavy ion accelerator, later into a lepton injector for LEP and now a high density proton injector for LHC.

The most important challenge for LHC is to discover, or exclude in a certain mass range, the Higgs particle and to search for supersymmetric particles. LHC may also discover new particles to manifest theories beyond the Standard Model.

There are four LHC experiments; CMS and ATLAS suited for general purpose experiments, LHCb devoted especially for b-physics and ALICE for heavy ion experiments. Their abbreviations are:

**ATLAS** A Toroidal Lhc ApparatuS [6].

**CMS** the Compact Muon Solenoid [7].

**ALICE** A Large Ion Collider Experiment [8].

**LHCb** (Study of CP violation in B-meson decays at LHC) [9].

---

[1] LHC has two separate rings; bunches are accelerated in both directions and they collide at the locations of the four detectors.

## 2.3 The ATLAS detector

The ATLAS detector, shown in figure 2.2, is the largest of the four LHC detectors. The cylindric shape measures 40 metres in length, has a radius of 10 metres and weighs 7000 tons. It is a general purpose experiment meant to look for many different signatures. A major role is to observe (or exclude) the Higgs boson and to look for supersymmetry.

The basic design criteria of the detector include the following [10]:

- Very good electromagnetic calorimetry for electron and photon identification and measurements, complemented by full-coverage hadronic calorimetry for accurate jet and missing transverse energy ($E_T^{miss}$) measurements;
- High-precision muon momentum measurements, with the capability to guarantee accurate measurements at the highest luminosity using the external muon spectrometer alone;
- Efficient tracking at high luminosity for high-$p_T$ measurements, electron and photon identification, $\tau$-lepton and heavy-flavor identification, and full event reconstruction capability at lower luminosity;
- Large acceptance in pseudorapidity ($\eta$) with almost full azimuthal angle ($\phi$) coverage everywhere. The azimuthal angle is measured around the beam axis, whereas pseudorapidity relates to the polar angle ($\theta$) where $\theta$ is the angle from the $z$ direction;
- Triggering and measurements of particles at low-$p_T$ thresholds providing high efficiencies for most physics processes of interest at LHC.

The ATLAS detector consists of four major components, the colours matching those in figure 2.2:

**Inner Detector** (yellow) - measures the momentum of each charged particle.

**Calorimeters** (electromagnetic; green, hadronic; orange) - measures the energies carried by the particles.

**Muon spectrometer** (blue) - identifies and measures muons.

**Magnet system** (grey) - bends charged particles for momentum measurement.

The following four sections describing the various parts of the ATLAS detector is based on the descriptions in the ATLAS Technical Design Report [10]. As for the different types of detector technologies (drift chambers, multi-wire proportional chambers etc.), consult [11] for further explanations and descriptions.

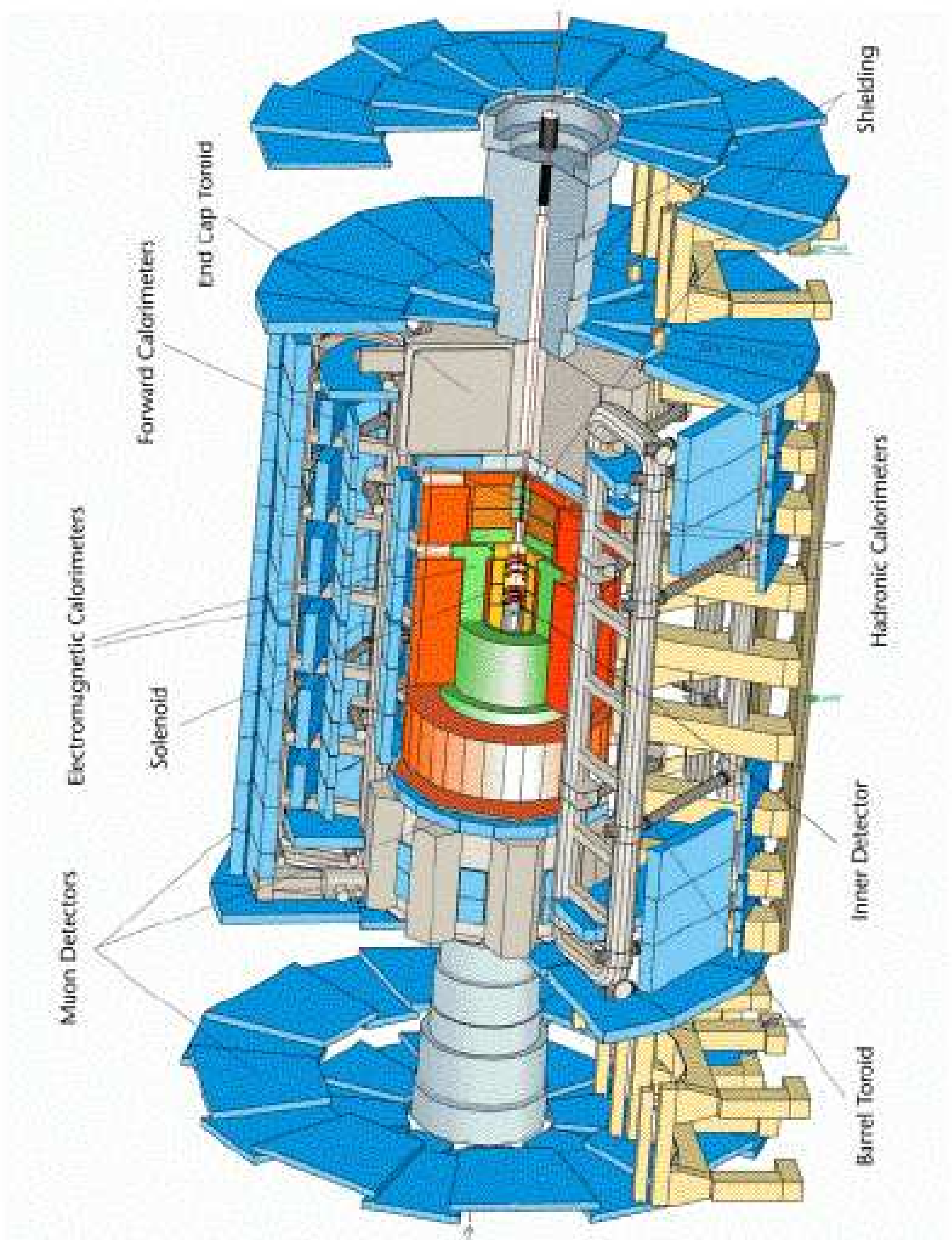

Figure 2.2: The ATLAS detector.

### 2.3.1 Inner Detector

The Inner Detector is the first part outside the beam-pipe and is contained within a cylinder of length 7 metres and a radius of 1.15 metres. We find high resolution semiconductor pixel and strip detectors in the inner part, and continuous straw-tube tracking detectors in its outer part as seen in figure 2.3. In the barrel region the detector layers are arranged on concentric cylinders around the beam axis, while the end-cap detectors are mounted on disks perpendicular to the beam axis.

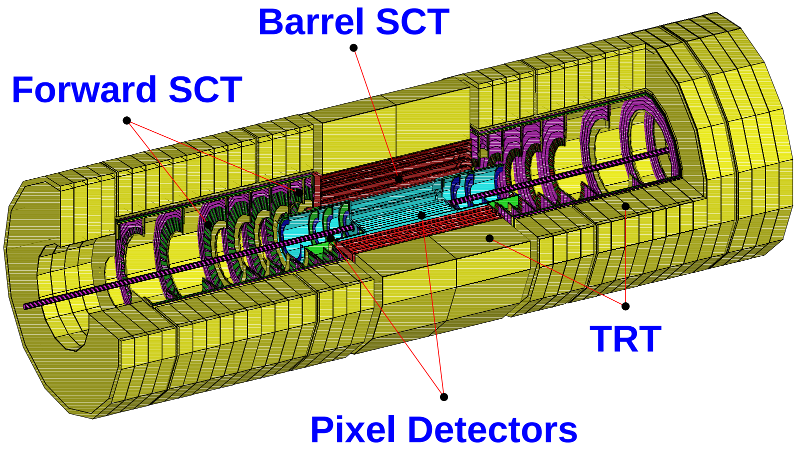

Figure 2.3: The ATLAS inner detector.

The pixel detector is designed to provide a high-granularity, high-precision set of measurements as close to the interaction point as possible. The total number of precision layers must be limited because of the material they introduce, and because of their high cost. In ATLAS, there are three pixel layers in the barrel region and five layers on the end-caps. The innermost pixel layer (the B-layer) is very important to maintain the highest possible performance during the experiment's lifetime, and the mechanical design allows for this to be replaced. The pixel system contains a total of 140 million detector elements contained in about 1500 barrel modules and 700 disk modules. Each element has individual circuits for each pixel element and the readout chips need to be radiation hardened to withstand over 300 kGy of ionising radiation and over $5 * 10^{14}$ neutrons per $cm^2$.

The semiconductor tracking system (SCT) is designed to provide eight precision measurements per track in the intermediate range, contributing to the measurement of momentum, impact parameter and vertex position, as well as providing good pattern recognition by the use of high granularity. The barrel SCT uses four layers of silicon microstrip detectors while the end-caps have nine on each side. Each silicon detector is 40.7 $cm^2$ and has 768 readout strips. Altogether, the detector contains 61 $m^2$ of silicon detectors with a total of 6.2 million readout channels. Tracks can be distinguished if separated by more than about 200 $\mu$m.

The transition radiation detector (TRT) provides continuous track-following with much less material per point and a lower cost. This high density of track hits at the outer radius contribute significantly to the momentum measurement, and is also valuable for the detection of photon conversions. The TRT is based on the use of straw detectors which can operate at the very high rate expected at the LHC. Each straw is 4 mm in diameter. The barrel contains about 50000 straws and the end-caps contain 320000 straws giving a total number of electronic channels of 420000. Each channel provides a drift-time measurement, giving a spatial resolution of 170 $\mu$m per straw. The TRT is operated with a non-flammable gas mixture of 70% Xe, 20% $CO_2$ and 10% $CF_4$, with a total volume of 3 $m^3$. The large amount of straws per track guarantees a combined measurement accuracy of better than 50 $\mu$m at the LHC design luminosity.

## 2.3.2 Calorimeters

The calorimeter system in figure 2.4 consists of an electromagnetic (EM) calorimeter outside the Inner Detector and out to a radius of 2.25 metres, and a hadronic calorimeter covering the area to a radius of 4.25 metres. The EM calorimeter is based on a highly-granular lead/liquid-argon (LAr) technology while the hadron calorimeter is based on a sampling technique with plastic scintillator plates (tiles) embedded in an iron absorber. The total weight of the calorimeter system is about 4000 tons.

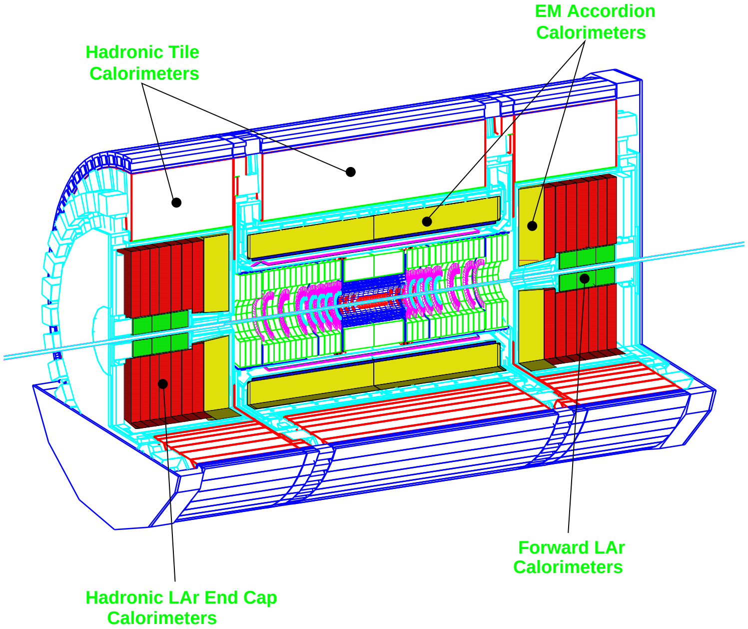

Figure 2.4: The ATLAS calorimeters.

The EM calorimeter is divided into a barrel part and two end-caps. The total thickness is >24 radiation lengths[2] ($X_0$) in the barrel and >26 $X_0$ in the end-caps. The lead LAr detector has accordion-shaped Kapton electrodes and lead absorber plates, the accordion geometry [12] provides complete $\phi$ symmetry. The region devoted to precision physics

---

[2] Radiation length is defined as the distance over which the electron energy is reduced by a factor 1/e due to radiation loss only.

($|\eta| < 2.5$) is segmented into three longitudinal sections. The inner one, the strip section, acts as a 'preshower' detector, enhancing particle identification ($\gamma/\pi^0$, $e/\pi$ separation, etc.) and providing a precise position measurement in $\eta$. For $|\eta| > 2.5$, the end-cap inner wheel, the calorimeter is segmented into two longitudinal sections and has a coarser lateral granularity. This is sufficient to satisfy the physics requirements (reconstruction of jets and measurement of $E_T^{miss}$). The region $1.37 < |\eta| < 1.52$ (the transition region between barrel and end-cap) is not used for precision physics measurements involving photons because of the large amount of material situated in front of the EM calorimeter.

The hadronic calorimeters cover the range $|\eta| < 4.9$ using different techniques best suited for the widely varying requirements and radiation environment over the large $\eta$-range. Over the range $|\eta| < 1.7$, the iron scintillation-tile technique is used. The scintillating tiles are 3 mm thick where two of the sides are read out into two separate photomultipliers. The total number of channels is about 10000. Over the range $1.5 < |\eta| < 4.9$, LAr calorimeters were chosen: the hadronic end-cap calorimeter (HEC) extends to $|\eta| < 3.2$, while the range $3.1 < |\eta| < 4.9$ is covered by the high-density forward calorimeter (FCAL). The HEC consists of two independent wheels built of 25 mm and 50 mm copper plates, each split into four drift spaces using three parallel electrodes. The FCAL is a particularly challenging detector owing to the high level of radiation it has to cope with. It consists of three sections, one made of copper and two of tungsten and LAr in the gaps in-between.

An important parameter in the design of the hadronic calorimeter is its thickness; it has to provide good containment for hadronic showers, and reduce punch-through into the muon system to a minimum. The total thickness is 11 interaction lengths[3] ($\lambda$). This is adequate to provide good resolution for high energy jets and good $E_T^{miss}$ measurement.

### 2.3.3 Muon spectrometer

The calorimeter is surrounded by the muon spectrometer. Excellent muon momentum resolution is achieved with three stations of high-precision tracking chambers, and multiple scattering is reduced due to a light and open structure. In the barrel region, tracks are measured in chambers arranged in three cylindrical layers (stations); in the end-cap region, the chambers are installed vertically, also in three stations. Over most of the $\eta$-range, a precision measurement of the track coordinates in the principal bending direction of the magnetic field is provided by Monitored Drift Tubes (MDTs). At large $\eta$s and close to the interaction point, Cathode Strip Chambers (CSCs) with higher granularity are used. The trigger system covers the pseudorapidity range $|\eta| \leq 2.4$; Resistive Plate Chambers (RPCs) are used in the barrel and Thin Gap Chambers (TGCs) in the end-cap regions. The overall layout of the muon chambers is shown in figure 2.5, which indicates the regions of the four different chamber technologies.

The basic detection elements of the MDT chambers are aluminium tubes with a central W-Re wire. Once a chamber is installed in its final location in the spectrometer, mechanical deformations are monitored by an in-plane optical system.

---

[3] Interaction length, also known as the 'mean free path', the mean distance travelled by the particle without suffering a collision.

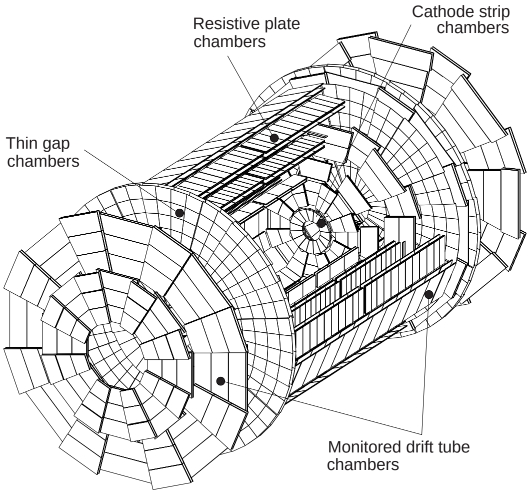

Figure 2.5: The ATLAS muon spectrometer.

The CSCs are multi-wire proportional chambers with cathode strip readout. The precision coordinate is obtained by measuring the charge induced on the segmented cathode by the avalanche formed on the anode wire. Good spatial resolution is achieved by segmentation of the readout cathode and by charge interpolation between neighbouring strips.

The basic RPS unit is a narrow gas gap formed by two parallel resistive Bakelite plates, separated by insulating spacers. Each chamber is made from two detector layers and four readout strips. The primary ionisation electrons are multiplied into avalanches by a high, uniform electric field.

The TGCs are similar in design to multi-wire proportional chambers. Signals from the anode wires provide the trigger information together with readout strips arranged orthogonal to the wires. These readout strips are also used to measure the second coordinate.

### 2.3.4 Magnet system

The ATLAS superconducting magnet system is an arrangement of a central solenoid (CS) providing the Inner Detector with magnetic field of 2 T, surrounded by a system of three large air-core toroids generating the magnetic field for the muon spectrometer. Each of the three toroids consists of eight coils assembled radially and symmetrically around the beam axis. Services are brought to the coils through a cryogenic ring linking the eight cryostats to a separate service cryostat, which provides connections to the power supply, the helium refrigerator, the vacuum systems and the control system.

### 2.3.5 Trigger and data-acquisition system

The interactions in the ATLAS detector will create an enormous data-flow. To digest this data we need:

**The trigger system** - selecting 100 interesting events per second out of 1000 million others. [13]

**The data acquisition system** - channeling the data from the detectors to the storage. [13]

**The computing system** - analysing 1000 million events recorded per year. [14]

# Chapter 3

# Theory

## 3.1 The Standard Model

The history of Particle Physics started with Democritus, a Greek philosopher (460-370 BC). He assumed that matter consisted of a few elementary particles; the atoms. This concept was developed further by Mendeleev, who in 1869 systematised the known elements into a Periodic Table. Today we believe in the Standard Model [15] where the fermions[1] are the building blocks of matter and the interactions are due to four fundamental forces; the electromagnetic, the strong, the weak and the gravitational force, mediated by the exchange of bosons.

The fundamental particles are the quarks, leptons and the gauge bosons. The quarks and the leptons (both fermions with spin 1/2) are divided into three families due to their characteristics. We call them the three generations of matter. The quarks are called: down, up, strange, charm, bottom and top,

$$\begin{pmatrix} u \\ d \end{pmatrix}, \begin{pmatrix} c \\ s \end{pmatrix}, \begin{pmatrix} t \\ b \end{pmatrix},$$

where the $u$, $c$ and $t$ have a charge of 2/3 e and the others -1/3 e. They exists in three different colours[2]: Red, Green and Blue. Bound systems consisting of three quarks (or three antiquarks), like the proton, the neutron or the lambda particle, are called baryons;

$$p(uud),\ n(udd),\ \Lambda(uds),$$

while quark-antiquark systems, for instance pions or kaons, are called mesons;

$$\pi^+(u\bar{d}),\ \pi^-(d\bar{u}),\ K^+(u\bar{s}),\ K^0(d\bar{s}).$$

The leptons can be split into three doublets:

$$\begin{pmatrix} \nu_e \\ e \end{pmatrix}, \begin{pmatrix} \nu_\mu \\ \mu \end{pmatrix}, \begin{pmatrix} \nu_\tau \\ \tau \end{pmatrix}$$

---

[1] Fermions are particles with half integer spin, bosons have integer spin.

[2] Colour having no analogy with true colours, they are simply another set of quantum numbers representing the charges of the strong force.

Here, the electron, muon and tau are very similar particles, however their masses are different. Their partners are the neutrinos which come in three different flavors: electron-neutrino, muon-neutrino and tau-neutrino. The neutrinos were for a long time believed to be massless. Only quite recent experiments [16] seem to show that they have a very small, but non-zero, mass. Both the three doublets of quarks and leptons have their anti-particles with the same properties but with opposite charge[3].

The force carriers for three of the fundamental forces (all except gravitation) are gauge bosons with spin one. The electromagnetic force carrier is the photon, a massless boson with no charge. The strong force, or QCD force, is mediated by gluons which come in eight different colour-anticolour combinations. The three heavy vector bosons $W^+$, $W^-$ and $Z^0$ are the force carriers of the weak force. One has managed to unify the weak and the electromagnetic force into the electro-weak theory. An effort is also being put into uniting the weak, electromagnetic and the strong force into a theory called GUT, Grand Unified Theory. As for the gravitational force, the least understood force, a force carrier is still not observed but assumed to be the Graviton.

An important aspect of the Standard Model is symmetries and the breaking of symmetries. It is a quantum field theory based on gauge, Lorentz and CPT[4] -invariance. The breaking of symmetries occur in connection with the Higgs boson, a still open question in the Standard Model of particle physics. In the Minimal Standard Model (MSM) there is only one Higgs boson while in other models there can be several. The next section is devoted to the theoretical foundation of the (MSM) Higgs boson.

Today there are some new theories which are beyond the Standard Model, for example supersymmetry[5], string theory and extra dimensions. The most common sypersymmetric model is the minimal supersymmetric model, MSSM, with five Higgs bosons, $H^+$, $H^-$, $A$, $H^0$ and $h$.

## 3.2 The Higgs mechanism

This section is based on a book of Halzen and Martin [17].

The Higgs mechanism [18] is best described in the framework of Lagrangian field theory. In classical mechanics, the equations of motion can be obtained from Lagrange's equations where the Lagrangian is $L \equiv T - V$ where $T$ and $V$ are the kinetic and potential energies of the system. This formalism can be extended from this discrete system to a continuous system:

$$L(q_i, \dot{q}_i, t) \to \mathcal{L}\left(\phi, \frac{\partial \phi}{\partial x_\mu}, x_\mu\right), \tag{3.1}$$

where $\mathcal{L}$ is the Lagrangian density

$$L = \int \mathcal{L} d^3x, \tag{3.2}$$

---

[3] Electrical charge as well as Lepton number, isospin, etc.

[4] Charge conjugation, parity and time inversion.

[5] All bosons have a identical fermion-twin and visa versa.

from now on simply referred to as the Lagrangian. The Euler-Lagrange equation replaces the Lagrange's equation from classical mechanics:

$$\frac{\partial}{\partial x_\mu}\left(\frac{\partial \mathcal{L}}{\partial(\partial\phi/\partial x_\mu)}\right) - \frac{\partial \mathcal{L}}{\partial \phi} = 0. \tag{3.3}$$

An example of a Lagrangian describing a free particle is:

$$\mathcal{L} = \frac{1}{2}(\partial_\mu\phi)(\partial^\mu\phi) - \frac{1}{2}m^2\phi^2. \tag{3.4}$$

We would now proceed to describe quantum field theory, and in order to do this the Lagrangian is quantised. Fields such as $\psi$ and $A_\mu$ become operators describing the creation and annihilation of particles, and the terms in the Lagrangian can be associated with propagators and vertex factors. It is then easy to translate the equations to Feynman diagrams.

Let us now turn our interest to $U(1)$ phase transformations[6] of the Lagrangian. A Lagrangian should be invariant under translations and transformations and especially under this internal symmetry transformation;

$$\psi(x) \to e^{i\alpha}\psi(x), \tag{3.5}$$

we call phase transformation where $\alpha$ is a real constant. Indeed the Lagrangian is invariant under this transformation, we speak of global gauge invariance. Global because $\alpha$ does not differ from space-time point to point. A more general invariance would then be a local gauge invariance, hence when $\alpha = \alpha(x)$. Equation (3.5) will then be generalised to

$$\psi(x) \to e^{i\alpha(x)}\psi(x) \tag{3.6}$$

where $\alpha(x)$ now depends on space and time in a completely arbitrary way. However the Lagrangian is not (yet) invariant and we will have to modify the derivative to what we call the covariant derivative

$$\partial_\mu \to D_\mu \equiv \partial_\mu - ieA_\mu, \tag{3.7}$$

where $A_\mu$ transforms as

$$A_\mu \to A_\mu + \frac{1}{e}\partial_\mu\alpha. \tag{3.8}$$

By demanding local gauge invariance we are forced to introduce this gauge field $A_\mu$. We can regard this as the physical photon field, but in that case we have to add a kinetic energy term to the Lagrangian. This term involves the gauge invariant field strength tensor

$$F_{\mu\nu} = \partial_\mu A_\nu - \partial_\nu A_\mu. \tag{3.9}$$

The Lagrangian of QED will then be

$$\mathcal{L} = \bar{\psi}(i\gamma^\mu\partial_\mu - m)\psi + e\bar{\psi}\gamma^\mu A_\mu\psi - \frac{1}{4}F_{\mu\nu}F^{\mu\nu}. \tag{3.10}$$

---

[6] The family of phase transformations forms a unitary Abelian group known as the $U(1)$ group.

In this equation there is no photon mass term $\frac{1}{2}m^2A_\mu A^\mu$ and the gauge particle must be massless. In QED and for the photon this is as it should be, but when we turn to weak interactions we get a similar result which gives us problems. Since the presence of mass terms for gauge fields destroy the gauge invariance of the Lagrangian; the $W$ and $Z$ bosons also have to be massless! But this is not the case. Experimentally these bosons have masses of the order of 100 GeV. Is it possible to introduce mass without breaking gauge invariance?

The answer is yes, and it leads us to the Higgs mechanism and the spontaneously broken symmetry. Let us first approach this by a populistic explanation by Tom Kibble [19]:

> *(...) The fundamental theory exhibits a beautiful symmetry between W, Z and photon. But this is a spontaneously broken symmetry. Spontaneous symmetry breaking is a ubiquitous phenomenon. For example, a pencil balanced on its tip shows complete rotational symmetry - it looks the same from every side. - but when it falls it must do in some particular direction, breaking the symmetry. We think the masses of the W and Z (and of the electron) arise through a similar mechanism. It is thought there are "pencils" throughout space, even in vacuum. (of course, these are not real physical pencils - they represent the "Higgs field" - nor is their direction a direction in real physical space, but the analogy is fairly close.) The pencils are all coupled together, so that they all tend to fall in the same direction. Their presence in the vacuum influences waves travelling through it. The waves have of course a direction in space, but they also have a "direction" in this conceptual space. In some "directions", waves have to move the pencils too, so they are more sluggish; those waves are the W and Z quanta. The theory can be tested, because it suggests that there should be another kind of wave, a wave in the pencils alone, where they are bouncing up and down. That wave is the Higgs particle.*

For a more formalistic approach we will here take the simplest example of the Higgs mechanism; regarding only $U(1)$ gauge symmetry. First we must make our Lagrangian invariant as we did in the previous example:

$$\phi(x) \to e^{i\alpha(x)}\phi(x) \tag{3.11}$$

requiring

$$D_\mu = \partial_\mu - ieA_\mu \tag{3.12}$$

and

$$A_\mu \to A_\mu + \frac{1}{e}\partial_\mu\alpha. \tag{3.13}$$

Now $A_\mu$ represents a vector boson in general. The gauge invariant Lagrangian is thus

$$\mathcal{L} = (\partial^\mu + ieA^\mu)\phi^*(\partial_\mu - ieA_\mu)\phi - \mu^2\phi^*\phi - \lambda(\phi^*\phi)^2 - \frac{1}{4}F_{\mu\nu}F^{\mu\nu}, \tag{3.14}$$

where $\phi$ is a complex scalar field $\phi = \frac{1}{\sqrt{2}}(\phi_1 + i\phi_2)$. If $\mu^2 > 0$ we will get the QED Lagrangian for a charged scalar particle of mass $\mu$. Since we want to generate masses by spontaneous symmetry breaking we take $\mu^2 < 0$ and $\lambda > 0$. We are now interested to find the minimum of the potential. To do this we must take the derivate with respect to $\phi$:

$$\frac{\partial V}{\partial \phi} = -\frac{\partial(\mu^2\phi^*\phi + \lambda(\phi^*\phi)^2)}{\partial \phi} = 0 \tag{3.15}$$

which satisfies

$$\phi_1^2 + \phi_2^2 = -\frac{\mu^2}{\lambda} \equiv v^2, \tag{3.16}$$

i.e. the potential has a circle of minima with radius $v$ in the $\phi_1$-$\phi_2$ plane. Now we choose the point $\phi_1 = v$ , $\phi_2 = 0$ as the ground state and we are spontaneously breaking the symmetry (in the same way the pencil balanced on its tip have to fall in one direction). We write

$$\phi = \frac{1}{\sqrt{2}}(v + \eta(x) + i\xi(x)) \tag{3.17}$$

where $\eta(x)$ and $\xi(x)$ represent the quantum fluctuations in the $\phi_1$ and $\phi_2$ plane respectively. Substituting (3.17) into the Lagrangian (3.14) we obtain

$$\mathcal{L}' = \frac{1}{2}(\partial_\mu\xi)^2 + \frac{1}{2}(\partial_\mu\eta)^2 - v^2\lambda\eta^2 + \frac{1}{2}e^2v^2A_\mu A^\mu - evA_\mu\partial^\mu\xi - \frac{1}{4}F_{\mu\nu}F^{\mu\nu} + ... \tag{3.18}$$

The particles in $\mathcal{L}'$ seems to be a Goldstone boson $\xi$, a scalar $\eta$, and a vector $A_\mu$, with masses

$$m_\xi = 0, m_\eta = \sqrt{2\lambda v^2}, m_A = ev.$$

We have achieved generating a mass to $A_\mu$ (remember, this is now a general vector boson) but are left with a massless Goldstone boson and a massive scalar ($\eta$) in addition. The solution for removing the Goldstone boson is to note that (3.17) can be reduced to

$$\phi \simeq \frac{1}{\sqrt{2}}(v + \eta)e^{i\xi/v} \tag{3.19}$$

in lowest order in $\xi$.

Let us now substitute a different set of real fields $h$, $\theta$, $A_\mu$ where

$$\phi \rightarrow \frac{1}{\sqrt{2}}(v + h(x))e^{i\theta(x)/v}, \tag{3.20}$$

and

$$A_\mu \rightarrow A_\mu + \frac{1}{ev}\partial_\mu\theta. \tag{3.21}$$

In this choice of gauge, $\theta(x)$ is chosen so that $h$ is real and we would expect that the theory will be independent of $\theta$. We obtain this Lagrangian:

$$\mathcal{L}'' = \frac{1}{2}(\partial_\mu h)^2 - v^2\lambda h^2 + \frac{1}{2}e^2v^2A_\mu^2 - v\lambda h^3 - \frac{1}{4}\lambda h^4 + \frac{1}{2}e^2A_\mu^2h^2 + ve^2A_\mu^2h - \frac{1}{4}F_{\mu\nu}F^{\mu\nu}. \tag{3.22}$$

Now the Goldstone boson is gone, we still have a massive $A_\mu$ and we have a Higgs boson in our theory.

If we repeat this procedure for a SU(2) gauge symmetry, $A_\mu$ will be the vector field $\mathbf{W}_\mu$ which represents the three vector bosons $W^+$, $W^-$ and $Z$. These bosons become massive, and that is the achievement we wanted. Here, $\phi$ is a doublet of complex scalar fields and after choosing the minimum and spontaneously breaking the symmetry we can substitute

$$\phi = \sqrt{\frac{1}{2}} \begin{pmatrix} 0 \\ v + h(x) \end{pmatrix} \tag{3.23}$$

where $h(x)$ is the Higgs field.

With the Higgs mechanism we have achieved to avoid massless particles. We have given mass to the heavy vector bosons and the fermions while still maintaining a massless photon. But why could we not have brutally broken the gauge invariance by inserting mass terms in the Lagrangian? Well, in that case we would not have had a renormalisable theory as we do with this spontaneously broken gauge theory.

# Chapter 4

# Software

## 4.1 Simulation software; PYTHIA and ATLFAST

PYTHIA [20] is a program which is frequently used for event generation in high-energy physics. The program is intended to generate complete events, in as much detail as experimentally observable ones, within the bounds of our current understanding of the underlaying physics.

In the analysis, ATLFAST [21] is invoked after PYTHIA and it is a program for fast detector simulation and physics analysis. It can be used for fast event-simulation including the most crucial detector aspects: jet reconstruction in the calorimeters, momentum/energy smearing for leptons and photons, magnetic field effects and missing transverse energy. Fast simulation is only an approximation of the real detector performance, for more accurate results one should run the full simulation. However, for this thesis I will only run the fast simulation, and it has the advantage of being less time and CPU consuming than the full simulation.

Both PYTHIA and ATLFAST are written in Fortran77. Within the ATLAS project there is a process going on of rewriting all the software into the object oriented language C++. This new software is still a little unpredictable, so for this analysis I have chosen to use the old and reliable software. But soon (hopefully) this transition phase will be over and the new software will be put to use.

Have a look at appendix A for detailed information of the parameters used in PYTHIA and ATLFAST for this analysis.

## 4.2 Parallel computing

Event simulation can be a time consuming and tiresome work, especially if one needs a large number of events. To cope with this situation I learnt to use MPI (Message Passing Interface) [22] and parallel computing. With this technique I could do jobs which usually took several days, over *one* night, using 15 computers in parallel. In order to use MPI one must have software installed (MPI compiler); the computers themselves are easily adapted for this use.

The simulation software, in my case PYTHIA, required only a few extra lines with code to adjust for the use of parallel computing. With this kind of event generation, the easiest is to let every computer take care of a fraction of the events. If one wants ten million events to run on ten machines, simply let each machine carry out one million events. The output will now be put into ten ntuple-files. An important thing to remember is to change the seed for the random generator, otherwise one will get ten identical ntuples.

## 4.3 Data analysis with PAW

CERN launched in 1986 the Physics Analysis Workstation project, PAW [23], an analysis software developed mainly for high energy physics applications. It is based on Fortran77 code, and in addition there exists a C++ version, PAW++.

The output from the simulations is a ntuple file. This file can be read by PAW and used further to plot and calculate various quantities (such as energy, transverse momentum, invariant two-photon mass, etc.). This can be done interactively by typing command line commands, by using a kumac-file (a file which contains PAW commands) or by Fortran or C programs. The plots are shown in an own window and can be stored as eps figures.

# Chapter 5

# Statistical methods

This chapter describes the statistical methods which I will use in the thesis. The main part is about calculating the significance in several ways, but also some aspects of mass reconstruction will be explained. At the end, an alternative approach with the ALRMC program is mentioned.

## 5.1 The significance

The significance of the signal is an important quantity. It tells whether there is a signal present in the histogram, or if it is only background. We typically say we have conclusive evidence for a signal if it is five sigmas or more.

The starting point of the significance calculation is to have a histogram which contains both signal and background in correct absolute and relative scaling. This histogram can be obtained from simulation or from data in a real experiment. In this thesis I will use two different methods to calculate the significance, the counting method and the chi-square method.

### 5.1.1 The counting method

The easiest and most straight forward approach of finding the significance of the signal is with a counting experiment. First, fit the S+B histogram with a Gaussian plus a polynomial, where the polynomial can be extracted as an approximation of the background. The significance is $S/\sqrt{B}$, and calculated using this formula:

$$s = \frac{N_{S+B} - B}{\sqrt{B}} \tag{5.1}$$

where $N_{S+B}$ is the total number of events in the histogram and $B$ the background events under the fitted background function, both in a given mass interval. The mass interval should be chosen in such a way that the significance is maximised.

The uncertainty in the calculation of the counting significance can be evaluated by taking the differential of $s = S/\sqrt{B}$. It is given by this formula:

$$(\Delta s)^2 = \left(\frac{\partial s}{\partial S}\Delta S\right)^2 + \left(\frac{\partial s}{\partial B}\Delta B\right)^2 \tag{5.2}$$

After some calculations and formula manipulations one ends up with

$$\Delta s = \sqrt{\left(\frac{\Delta S}{\sqrt{B}}\right)^2 + \frac{S^2(\Delta B)^2}{4B^3}} \sim \frac{\Delta S}{\sqrt{B}}. \tag{5.3}$$

The approximation is valid in cases where $S \ll B$, as for this channel. The error $\Delta S$ can be calculated with respect of the errors $\Delta N_{S+B}$ and $\Delta B$. However for the analysis it is very convenient to use the output from PAW, where the fitted number of signal events with uncertainties comes directly from the fitting procedure.

### 5.1.2 The chi-square method

The chi-square method for calculating the significance gives a better approximation to the real signal. The contribution from the signal is not cut using sharp borders like in the counting method, but corresponds to the fit of the whole signal range.

Begin with applying the best fit to the signal plus background histogram, using a combination of a Gaussian and a polynomial (or exponential). This is easily done with PAW or other analysing software. The output from the fitting is a $\chi^2_{S+B}$, a quantity dependent on the difference of the histogram and the function in each bin (see equation (5.4)). Now, take the fitted function and extract the background part, that is only the polynomial (without the Gaussian). Calculate a $\chi^2_B$ using the histogram and the background function. Note that you are not trying to minimise the $\chi^2$ this time, but simply to calculate it by the standard formula:

$$\chi^2 = \sum_{i=1}^{nbins} \frac{(y^i_{hist} - y^i_{fit})^2}{\sigma_i^2}, \tag{5.4}$$

where $\sigma_i$ is the standard error in each bin (poisson distribution), $\sqrt{y^i_{fit}}$.

Another useful quantity is the number of degrees of freedom, *d.o.f.*, which is defined as

$$d.o.f. = \#bins - \#parameters - 1 \tag{5.5}$$

where *#parameters* is the number of parameters in the fitted function.

One should now make a test of whether to accept the S+B hypothesis (the hypothesis saying there is actually a signal present and not only background) or not. The requirement is that

$$\chi^2_{S+B}/d.o.f. \tag{5.6}$$

should be roughly one, and

$$\chi^2_B/d.o.f. \tag{5.7}$$

should be somewhat larger. How much larger depends on the amount of events in the histogram. What you actually do in this test is to ask: Which of the functions can best fit my histogram? Is it the one with a signal, or the one without?

Finally, calculate a $\Delta\chi^2$ by subtracting the two $\chi^2$'s:

$$\Delta\chi^2 = \chi^2_B - \chi^2_{S+B}. \tag{5.8}$$

This variable is the basis of the significance calculation, and one can look at statistical tables or use programs which transforms the $\Delta\chi^2$ to probability and to number of sigmas. The number of degrees of freedom is in this case one, which is the Higgs mass (the Standard Model cross-section is again dependent on the mass). However, in this case with only one *d.o.f.* one can get the significance by simply taking the square root of $\Delta\chi^2$. This is because the p.d.f. of the $\chi^2$ distribution for *d.o.f.* $= 1$ is the normal distribution.

## 5.2 The significance with two channels

The idea is that splitting the events into two independent channels will increase the significance of the signal. This concept can be used if the resolutions of the two channels are different, otherwise one would not gain from it. Assuming the same number of signal events, a narrow and high top (good resolution) will have a greater contribution for the significance than a wide and low top (bad resolution). This is because the relative uncertainty is less the more events in a bin. The signal resolution for one channel is necessarily worse than the best of the two with two channels. So by using two channels, the information obtained from the simulation is better utilised, and the method is more optimal.

A possibility is to split the data into events with unconverted photons (1) and events with one or more converted photon(s) (2). As shall be investigated later, the resolutions for converted photons and unconverted are different, so the method is valid. To use this approach, one has to make two histograms with signal plus background, and do the significance calculation on both.

One could also think of splitting it into three channels; unconverted photons, one converted photon and two converted photons. These three channels will also have different resolutions, but the problem is that there would be too few events in the histogram containing two converted photons (the probability of two converted photons is about 15%). However this is a good idea when the statistics are high enough.

### 5.2.1 The counting method

The significance from the two channels in a counting experiment is combined using:

$$s_{12} = \frac{S_1 + S_2}{\sqrt{B_1 + B_2}}, \tag{5.9}$$

where $S_i = N_i^{S+B} - B_i$ for $i = 1, 2$, and the uncertainty with:

$$(\Delta s_{12})^2 = (\Delta s_1)^2 + (\Delta s_2)^2. \tag{5.10}$$

### 5.2.2 The chi-square method

After following the procedure of finding the chi-squares on the two histograms (as described earlier), one will end up with four quantities; two values for $\chi^2_{S+B}$ and two for $\chi^2_B$. Since having two channels would be equivalent to increasing the number of bins to twice as many, the $\chi^2$'s for case 1 and 2 should be added. This gives:

$$\Delta\chi^2_{12} = (\chi^2_{B,1} + \chi^2_{B,2}) - (\chi^2_{S+B,1} + \chi^2_{S+B,2}). \tag{5.11}$$

Again, take the square root of this number to get the significance of the signal.

## 5.3 The Higgs mass and its uncertainty with two channels

From the two histograms (1 and 2) with signal and background, one can make a combined calculation of the Higgs mass:

$$M = \frac{\frac{m_1}{\sigma_1^2} + \frac{m_2}{\sigma_2^2}}{\frac{1}{\sigma_1^2} + \frac{1}{\sigma_2^2}} \tag{5.12}$$

with an uncertainty given by

$$\frac{1}{\sigma_M^2} = \frac{1}{\sigma_1^2} + \frac{1}{\sigma_2^2}. \tag{5.13}$$

Here, 1 and 2 denotes the histograms of the two channels, $m_1$ and $m_2$ the mean value of the fitted signal (the Gaussian), and $\sigma^2$ the uncertainty in the mean.

## 5.4 ALRMC

ALRMC[1] is a statistical program which is used for Higgs search on LEP [24] data. Like the chi-square method, ALRMC is using a technique which takes into account all the events under the signal p.d.f. and in addition, the bins are weighted after the amount of signal events. That means, the weight from the bin in the middle of the signal is larger than from the tail, and the weight from where there is no signal, is zero.

When I started on this thesis I thought I could use the program for statistical treatment of my data. However, it turned out that the program was not well suited for analysis of data with statistics as high as in this channel[2]. So the conclusion was that I would make

---

[1] Abbreviation for A Likelihood Ratio Monte Carlo.

[2] ALRMC calculates each candidate for signal and background separately, and this would not be efficient since there are over 1000 signal events and ten thousands of background events.

another algorithm for finding the significance, as explained in the previous sections. These days, there is an ongoing process of translating ALRMC from Fortran77 into C++, and of improving it. After this transition phase, it is expected to perform better with the high statistics cases. So when the new version is up and running it would (probably) be possible to use in this type of experiment.

Since I am not using the program for this analysis, I will not try to explain the methods used in the program. The readers that are interested will find information in reference [25, (available after August 2002)]. In addition, a master thesis [26] has been devoted to the process of translating the program, and this thesis is perhaps a more pedagogically approach to understand the program. It contains both the theoretical foundation, and explanation of how this is used numerically.

# Chapter 6

# The analysis

This chapter is devoted to some essential background information about the analysis. I will present some of the knowledge LHC inherited from the LEP experiments, some general LHC Higgs search facts and detailed information about the signal and background processes in this particular channel. Finally I will make a few comments about photon conversions and radions.

## 6.1 The heritage from LEP

LEP completed data-taking in November 2000 after 11 years of running. In 2000 the centre-of-mass energy was pushed to 209 GeV and in the last three years a luminosity of about 687 $\text{pb}^{-1}$ was delivered to each of the four experiments. One of the goals of the project was to search for a Standard Model Higgs boson. Their achievement was to exclude a Higgs boson below a mass of 114.1 GeV[1] at 95 % Confidence Level [27] (the shaded area in figure 6.1). Even if the SM Higgs cross-section is reduced by a factor three, a Higgs boson mass up to 110 GeV is excluded. In addition to the important exclusion limit, the four LEP experiments also gave a significance of 2.1 sigmas for a Higgs boson with a mass of 115 GeV. This is not enough for discovery, but can be interpreted as a hint of a Higgs boson in that mass region.

Figure 6.1 shows the best fit of the Standard Model to the LEP data. Minimum $\chi^2$ is found for $m_H = 88^{+35}_{-45}$ GeV, and $m_H < 196$ GeV at 95% C.L.

## 6.2 Higgs search at LHC

The production of the Standard Model Higgs boson at LHC is expected to proceed mainly through the diagrams shown in figure 6.2. The cross-sections for these processes are shown in the same figure (left) as a function of the Higgs mass. The gluon-gluon fusion process is the dominant production channel for all masses, but for $m_H \sim 1$ TeV

---

[1] Natural units, i.e. the convention $\hbar$=1, $c$=1 is used throughout this document.

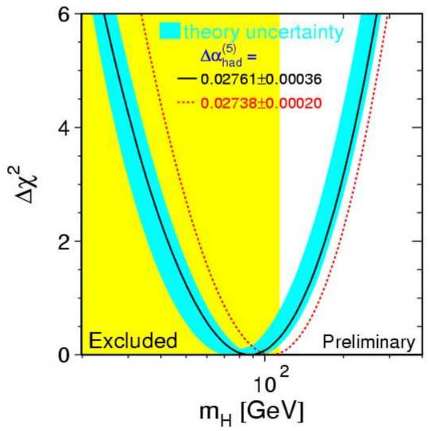

Figure 6.1: The LEP Higgs boson mass exclusion limit.

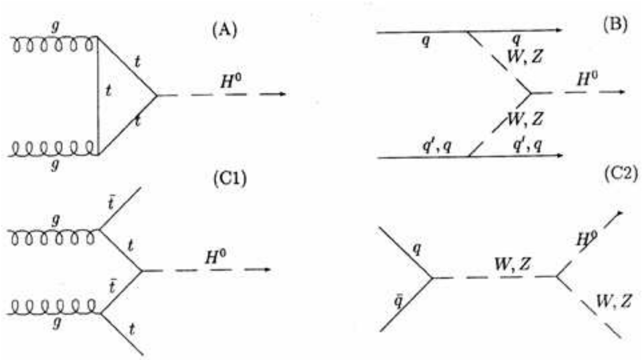

Figure 6.2: Feynman diagrams of the Higgs production processes.

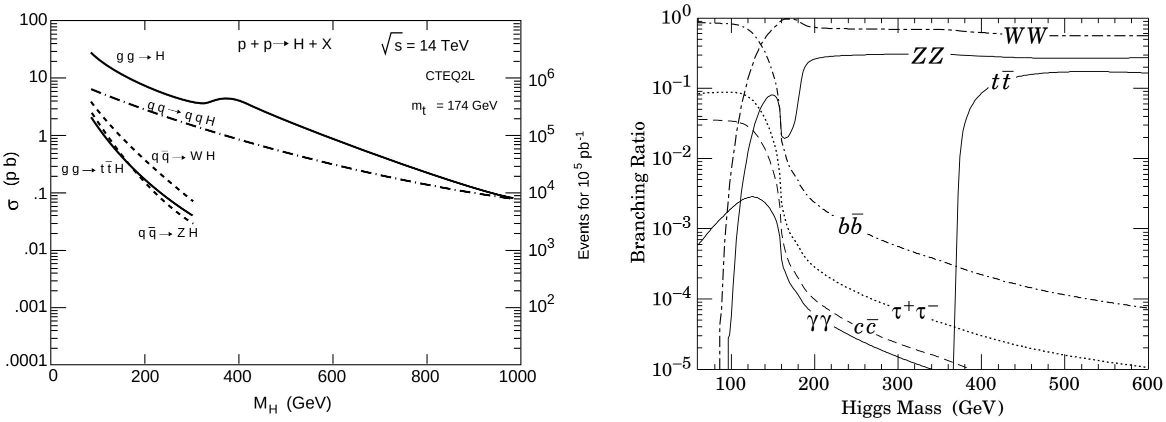

Figure 6.3: Higgs production cross-section (left) and Higgs branching ratios (right) both as a function of the Higgs mass.

it is similar in magnitude to the vector boson (WW, ZZ) fusion. The associated Higgs production with a $t\bar{t}$ pair or a $W/Z$ boson has a significantly smaller cross-section, however, it gives rise to final states which are relatively easy to extract from the background, thanks to the additional signature (for instance leptons) produced in the decay of the accompanying particles.

All the decay branching ratios of the Higgs boson are in figure 6.3 (right), where three main regions can be identified:

- $\mathbf{m_H < 130GeV}$: $H \to b\bar{b}$ dominates, however, because of its huge QCD background ($N_S/N_B < 10^{-5}$), $H \to \gamma\gamma$ is the most promising channel.
- $\mathbf{130GeV < m_H < 2m_Z}$: $H \to WW^* \to l\nu\, l\nu$ and $H \to ZZ^* \to ll\, ll$, where one of the vector bosons can be virtual, are the only two channels which can be extracted from the background in this region.
- $\mathbf{m_H > 2m_Z}$: $H \to ZZ, WW \to$ combinations of $l, \nu$ and jets. The process $H \to ZZ \to ll\, ll$ is called the *gold plated channel*, with almost no background.

The Standard Model does not predict the mass of the Higgs boson, so we have to look in all the mass ranges. The only prediction it gives us is that we have a theoretical upper bound of $\sim$ 1 TeV (because of consistency arguments within SM [28]).

The LHC expects to operate at a centre-of-mass energy of $\sqrt{s} = 14$ TeV. References on Higgs searches at LHC are [2] and [29]. Reference [30] is an analysis of the impact of the sensitivity for different values of the centre-of-mass energy.

## 6.3 $H \to \gamma\gamma$

The channel of the Higgs particle decaying into a pair of photons will be an important one at the LHC. It is the most promising channel to observe a light Higgs boson with a mass of the order $80 - 150$ GeV. The channel has a small branching ratio, only about 0.2%, which means that the Higgs rarely decays into two photons. However, when it does, it is a clean channel with a signal to background ratio of $N_S/N_B \sim 10^{-2}$.

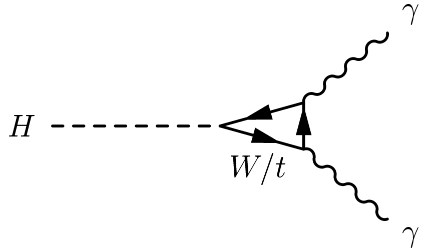

Figure 6.4: $H \to \gamma\gamma$ Feynman diagram.

The Feynman diagram of the signal is shown in figure 6.4. The Higgs boson decays into two $W$'s or a $t\,\bar{t}$ pair, which interacts and creates two photons in the final state. In my analysis I will look for a Higgs mass between 120 and 150 GeV (the lower limit because of the LEP exclusion).

For my analysis I have chosen to only look at the direct $H \to \gamma\gamma$ channel. This means I will omit the associated Higgs production processes (C1 and C2 in figure 6.2). These processes have a cross-section which is almost a factor 50 lower than for the direct production, but is easier to extract because of the additional particle in the final state.

Severe requirements on the performance of the EM Calorimeter are placed by this channel. Excellent energy and angular resolution are needed to observe the narrow mass peak and powerful particle identification capability is also required to reject the large QCD jet background.

## 6.4 Background

The background of $H \to \gamma\gamma$ is events produced within the Standard Model which consists of two photons in the final state. We have events which we are able to suppress (the reducible) and some we are not (the irreducible).

### 6.4.1 Irreducible; Born and box reactions

The irreducible background consists of reactions with fermions or gluons which interact and produce two photons as the final state. The dominating processes are the Born and the box processes, their reactions are:

$$Born : f\bar{f} \longrightarrow \gamma\gamma$$

$$Box : gg \longrightarrow \gamma\gamma$$

The Feynman diagrams are shown in figure 6.5.

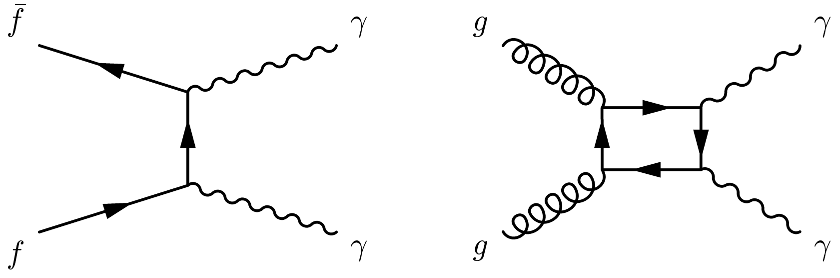

Figure 6.5: Born and box Feynman diagrams, irreducible background.

### 6.4.2 Irreducible; Bremsstrahlung reactions

In addition we have some events with only one photon plus one fermion/gluon in the final state. The fermion/gluon can then emit another photon through bremsstrahlung, giving a softer photon. The reactions can be as follows;

$$f\bar{f} \longrightarrow g\gamma \rightsquigarrow g\gamma\gamma$$

$$fg \longrightarrow f\gamma \rightsquigarrow f\gamma\gamma$$

$$gg \longrightarrow g\gamma \rightsquigarrow g\gamma\gamma$$

The second of these processes is drawn in figure 6.6.

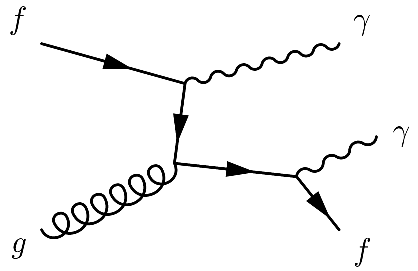

Figure 6.6: One of the bremsstrahlung Feynman diagrams, irreducible background.

In the analysis done for the ATLAS TDR [2], this background was not simulated but calculated with some matrix element calculation in the early 90s [31]. The result from this calculation is that the Bremsstrahlung background amounts to about 50% of the combined Born plus box contribution. In the ATLAS analysis, this contribution is included in the simulations by correspondingly scaling the Born and box background.

### 6.4.3 Reducible

In addition to the irreducible $\gamma\gamma$ background, the QCD jet-$\gamma$ and jet-jet background have to be considered. This is events where one or both jets are misidentified as photons. Since the production cross-sections for these processes are many orders of magnitude larger than the signal cross-section, it is possible to suppress this background by obtaining excellent photon/jet and photon/electron discrimination in the detector. The ratios of the cross-sections for jet-$\gamma$ and jet-jet to the irreducible $\gamma\gamma$ are $2 * 10^6$ and $8 * 10^2$ respectively [2]. After rejection of most of these events in the calorimeter they each amounts of about 20% of the total irreducible background.

For Higgs masses close to the Z mass ($m_Z$ = 91 GeV) the resonant background from $Z \rightarrow ee$ decays have to be taken into account. However, in this thesis I am looking for a Higgs mass between 120 and 150 GeV so I can safely ignore this contribution (anyway it would be negligible even when looking at a Higgs mass of 90 GeV [2]).

## 6.5 EM Calorimeter performance - Photon conversions

This subject is thoroughly described in the TDR [10]. Here I will only state some facts that are important for my analysis.

Because of the significant amount of material in front of the calorimeters, many of the photons are converted. Since the $H \to \gamma\gamma$ signal is small, it is essential to ensure high efficiency, and consequently to recover the conversions. Around 30 % of all photons convert in the material of the ID cavity. In figure 6.7 the fraction of converted photons as a function of pseudorapidity is shown. Around 75 % of the conversions occur inside the volume[2] $R_c$ <80 cm, $|z_c|$ <280 cm.

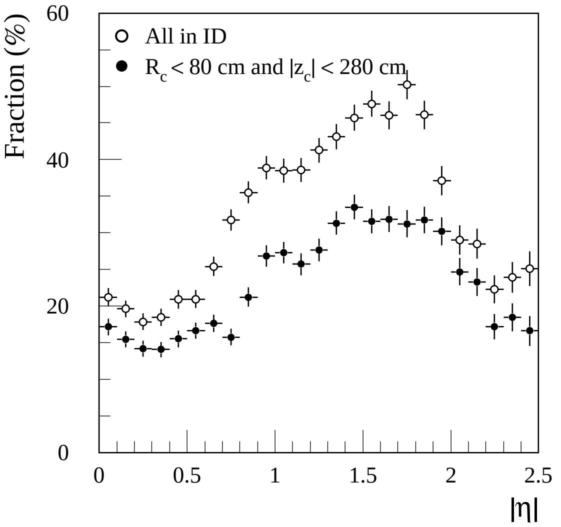

Figure 6.7: Fraction of converted photons as a function of pseudorapidity.

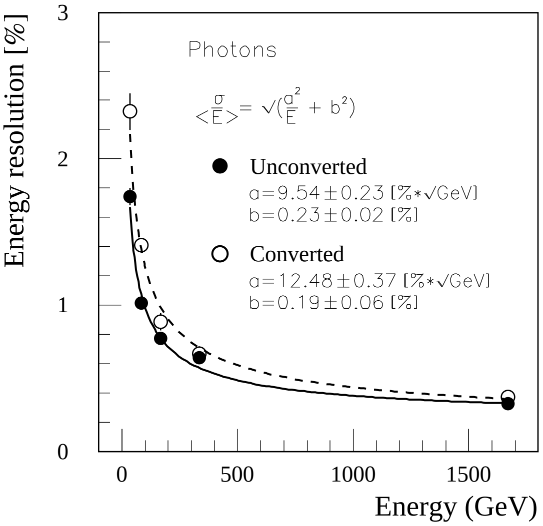

Figure 6.8: Energy resolution for converted and unconverted photons at $\eta = 1.1$, as a function of the photon energy.

The resolution of the electromagnetic calorimeter at $\eta = 1.1$ is given in figure 6.8 as a function of the photon energy. For a photon in the range up to 200 GeV, the energy resolution for converted is significantly worse (higher) than for the unconverted photons. For the higher energies, the difference is smaller.

Photon conversions are found by combining pairs of oppositely charged electron/positron tracks, and the smallest possible cluster[3] is needed to reduce the contribution of the pile-up[4] and electronic noise to the energy resolution. On the other hand, a relatively large cluster is needed to fully contain the shower in order to limit the impact of lateral fluctuations on the energy resolution. The cluster size depends on the particle type, energy

---

[2] $R$ is a coordinat in the pseudorapidity-azimuthal angle space ($R = \sqrt{\eta^2 + \phi^2}$), while $z$ is along the beam axis.

[3] Energy depositions in neighbouring elements are grouped into energy clusters. Each cluster is associated an energy, a radial and azimuthal coordinate and a cluster size.

[4] Pile-up happens if an event arrives the detector while the detector is still processing the previous event. The result is a distortion of the signal.

and pseudorapidity. Electron reconstruction needs larger clusters than photons because of their larger interaction probability in the upstream material and in the presence of a magnetic field, and as a result, this gives a worse energy resolution.

The overall photon identification efficiency with the ATLAS detector is found to be about 80 %.

## 6.6 Radions

This section is based on talks given by Per Osland [32]. I will not give a thorough presentation, but simply state some facts and show a few plots.

Radions are particles associated with the $\phi$ field within string theory. They appear in the Randall-Sundrum scenario [33] where the universe is (4+1) dimensional. The radion and the Higgs are particles which look very much alike, having similar characteristics and interactions. This is important to have in mind during Higgs search, and if extra dimensional particles do exist, we should learn to differentiate between the two of them.

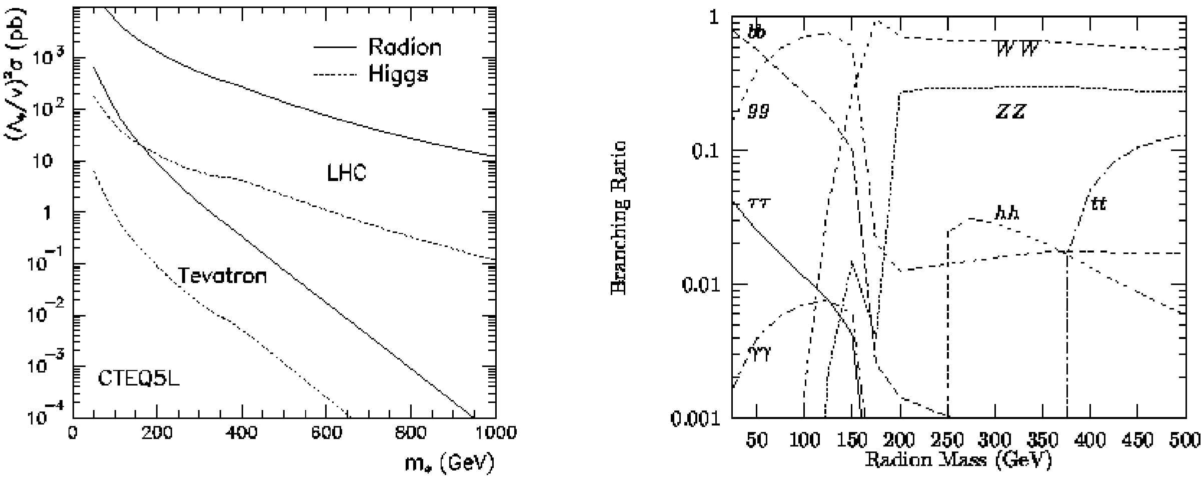

Figure 6.9: Production cross-section for the (SM) Higgs and the radion at LHC and Tevatron (left) and branching ratio for the radion (right), both as a function of the radion ($\phi$) mass.

The radions are produced mainly by the gluon-gluon fusion process, and the cross-section is about 100 times larger than for the Higgs boson (figure 6.9 (left)). They have nearly the same decay channels, arranged by branching ratio in figure 6.9 (right). Note that in addition to the Higgs channels, the radions can also decay into two Higgs bosons. That is if the radion appears to be a good deal heavier than the Higgs boson.

The $\gamma\gamma$ decay rate for the radion is almost twice the rate of the Higgs as shown in figure 6.10. This means that in this channel, the frequency of actually observing a radion will be larger than observing a Higgs (if they exist).

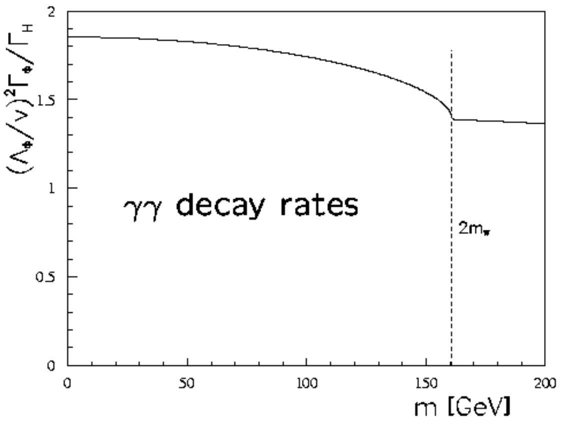

Figure 6.10: Ratios of the $\gamma\gamma$ decay rates $(\Gamma_{\phi\to\gamma\gamma}/\Gamma_{H\to\gamma\gamma})$ as a function of the radion/Higgs mass.

# Chapter 7

# Results

This chapter presents the results from the analysis. First, the signal (the process $H \to \gamma\gamma$) and background (all other processes with $\gamma\gamma$ in the final state) are reconstructed, then they are applied on the same histogram to illustrate data from a real experiment. On this S+B histogram, the significance of the signal is calculated. This is a measure of whether a particle can be observed or not. Finally, the outcome from my analysis is discussed and put in a larger context.

## 7.1 Cuts

The cuts applied to both signal and background throughout this analysis are:

- **$|\eta| < 2.4$, and no photons in the barrel/end-cap transition region $1.37 < |\eta| < 1.52$**: This is the region suited for precision physics due to the construction of the electromagnetic calorimeter.

- **$P_T(1) > 40$GeV and $P_T(2) > 25$GeV:** This is the lower limits of the transverse momenta of the two photons.

In addition, another cut has been introduced in section 7.3.2.

## 7.2 Signal reconstruction

The production cross-section times branching ratio for $H \to \gamma\gamma$ is slightly below 50 fb (46 fb at 120 GeV). It varies with the Higgs mass and peaks around 120 GeV as in figure 7.1. The plot is made using 15 runs with ATLFAST, one for every 5 GeV at high luminosity and 1000 events. The shape of the curve is dictated by the branching ratio curve in figure 6.3, having the same shape and a maximum at a Higgs mass about 120 GeV.

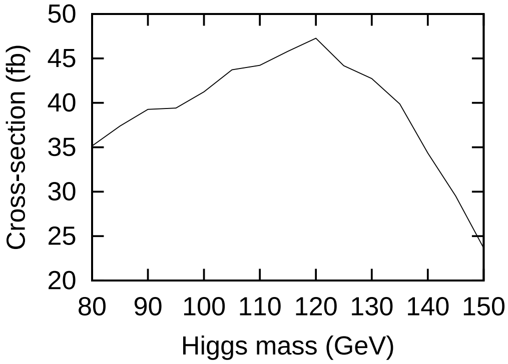

Figure 7.1: Cross-section times branching ratio for $H \to \gamma\gamma$ as a function of Higgs mass.

The Higgs production processes are described in section 6.2. The four processes in table 7.1 are the most important (the ISUB number are used in PYTHIA). They corresponds to the processes A and B in figure 6.2. Process 3 contains contributions from all flavours, but is completely dominated by the subprocess $t\bar{t} \to H$. The process-ratios in table 7.1 are for a Higgs mass of 120 GeV, and they are stable within the mass range to 150 GeV.

| ISUB | Process | Ratio (%) |
|---|---|---|
| 3 | $f\bar{f} \to H$ | 6.1 |
| 102 | $gg \to H$ | 72.0 |
| 123 | $ff \to ffH$ ($ZZ$ fusion) | 5.9 |
| 124 | $ff \to ffH$ ($W^+W^-$ fusion) | 16.0 |

Table 7.1: The ratios of the different Higgs production processes at a Higgs mass of 120 GeV.

The fast simulation, ATLFAST, does not handle converted photons, only full simulation does. So for my analysis, I have studied the behaviour of the converted photons as described in the TDR [10], and tried to fake them. The algorithm for doing this has its origin in figure 6.7, I simply used this probability of converted photons at a given pseudorapidity. In addition, the energy deposited by the converted photons gives a large tail on the low energy side, meaning the converted photons will peak at a slightly smaller two-photon mass than the unconverted ones. After reducing the two-photon invariant mass with 0.3 GeV on the events containing at least one converted photon, the faked converted photon events looks very much like the fully simulated ones described in the TDR.

Figure 7.2 shows the reconstructed signal for a Higgs mass of 120 GeV, consisting of the unconverted photon events directly from ATLFAST and the faked converted ones (shaded). The shape of the signal from the reconstruction in ATLFAST is a Gaussian with a width that reflects the resolution of the electromagnetic calorimeter. For the Higgs at 120 GeV the resolutions for the converted and unconverted channels are $\sigma_{conv} =$ 1.37 GeV and $\sigma_{unconv} = 1.32$ GeV, both with an uncertainty of 0.03 GeV (from the output of paw). The fact that the two resolutions are observed different, and that the converted

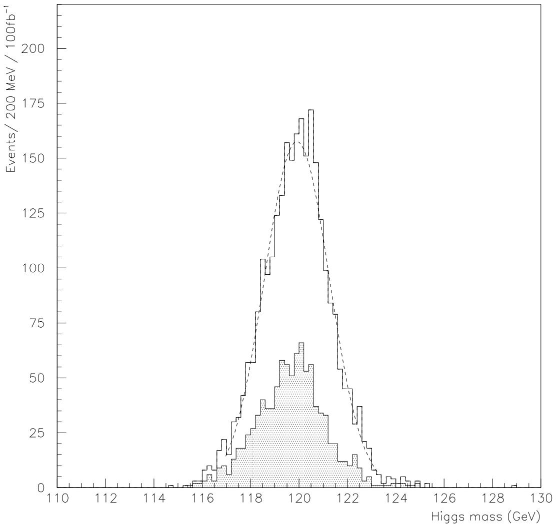

Figure 7.2: Reconstructed two-photon invariant mass with $m_H = 120$ GeV for high luminosity. The shaded area represents events containing at least one converted photon. The fitted width of the total signal is $\sigma = 1.34$ GeV.

case is the worse is in agreement with figure 6.8. However, this difference is not large, and the uncertainties are overlapping each other. The total signal (both unconverted and converted events) has a fitted width and a resolution of $\sigma = 1.34$ GeV.

The number of events in the histogram is given by the standard formula

$$N = \sigma \mathcal{L} \epsilon, \tag{7.1}$$

where $\sigma$ is the cross-section and $\mathcal{L}$ the integrated luminosity. $\epsilon$ is the efficiency $\epsilon = \epsilon_{photon}\epsilon_{cuts}$ where $\epsilon_{photon} = 0.64$ (0.8 for each photon) and $\epsilon_{cuts}$ is the efficiency of the cuts in the analysis listed in table 7.2. The efficiencies in the table are the values obtained through the event generation.

| **Higgs mass (GeV)** | **120** | **130** | **140** | **150** |
|---|---|---|---|---|
| $\epsilon_{cuts}$ | 0.59 | 0.61 | 0.62 | 0.63 |
| Mass resolution (GeV) | 1.34 | 1.42 | 1.49 | 1.53 |

Table 7.2: Efficiency of cuts and the mass resolution of the signal at four Higgs masses.

## 7.3 Background reconstruction

### 7.3.1 Born and box

The production cross-section for the Born and box processes are $\sigma_{bb} = 0.65$ pb for an invariant two photon mass at 120 GeV, and are distributed for other masses in figure 7.3[1]. The total (integrated) cross-section for the range 100-150 GeV is 29 pb and for the range 120-170 GeV, 16 pb. These are the two ranges used in my analysis.

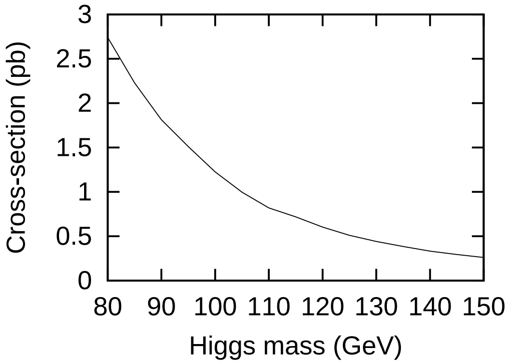

Figure 7.3: Cross-section for the combined Born and box background processes as a function of invariant two-photon mass.

The Born plus box background distribution is shown in figure 7.4, the contribution from Born slightly larger than box. The total distribution can be fitted well with a polynomial of order 3. Again, the number of events in the histogram is given with equation 7.1 with an efficiency of cuts $\epsilon_{cuts} \sim 0.18$ in both ranges (100-150 GeV and 120-170 GeV). If we apply the (faked) converted photons to the background as well, using the same algorithm as for the signal, the distributions are as shown in figure 7.5. The converted photons amounts to about $30-40\%$ of the unconverted ones.

### 7.3.2 Bremsstrahlung

In spite of that the quark bremsstrahlung processes was not simulated for the TDR, I wanted to see if ATLFAST could reproduce this 50% *of the Born plus box background* result.

The production cross-section for the bremsstrahlung background (from the output of ATLFAST) for the range of two-photon mass between 100 and 150 GeV is of the order $10^{-8}$ b. That means, while I at low luminosity needed to produce some hundred thousand events of the Born plus box background I will need some hundred million events of the bremsstrahlung. After production of the events, less than a thousandth passes through the selection criteria.

---

[1] The plot is done the same way as for the signal, 1000 simulated events for every 5 GeV.

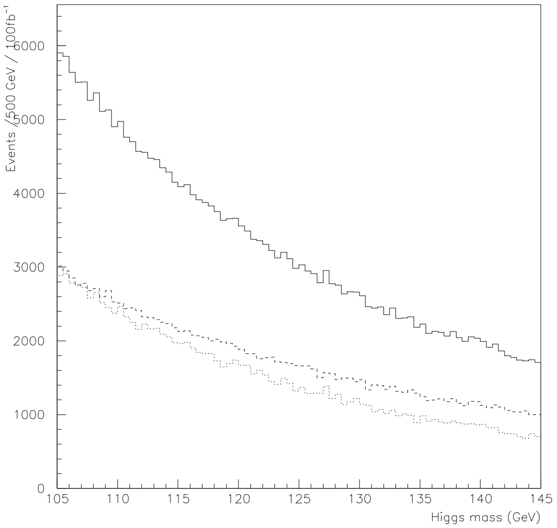

Figure 7.4: The unconverted photon contribution from the Born (dotted) and box (dashed) backgrounds and the sum of these (line) as a function of invariant two-photon mass at high luminosity.

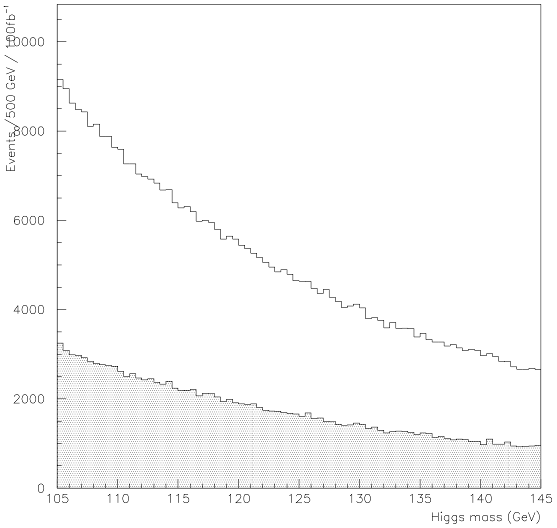

Figure 7.5: The total Born plus box background as a function of invariant two-photon mass at high luminosity. The areas represent events with at least one converted photon (shaded) and events without conversions (the white area).

With only the cuts described in section 7.1, the amount of bremsstrahlung events is 5-6 times larger than that of the Born and box (see figure 7.7). So, I had to introduce other cut parameters in order to reduce the bremsstrahlung. I ended up using a $P_T$ balance cut:

$$P_T^{balance} = \frac{P_{T,1}}{P_{T,1} + P_{T,2}} \tag{7.2}$$

where 1 and 2 are the two photons in the final state, arranged by decreasing $P_T$. This parameter is plotted in figure 7.6 for the bremsstrahlung, Born plus box and signal. From the figure it is quite obvious that the bremsstrahlung can be reduced drastically when cutting on high $P_T^{balance}$ values. In figure 7.7 the impact on the bremsstrahlung background for the cuts $P_T^{balance} \leq 0.95$, 0.90, 0.85, 0.80, 0.75 and 0.70 is shown. The Born plus box background is not reduced noticeably when introducing these cuts. Using the strongest cut, the bremsstrahlung/Born plus box ratio is around two. Unfortunately the signal is loosing events because of the cut, and this is important to avoid since the signal is quite small for this channel.

The number of bremsstrahlung, Born plus box and signal events is reduced due to the $P_T^{balance}$ cut in a manner described in table 7.3. Note that I have been using different luminosities for the background processes (7 fb$^{-1}$) and the signal (100 fb$^{-1}$). With these results we would expect the significance ($S/\sqrt{B}$) to decrease with a stronger cut.

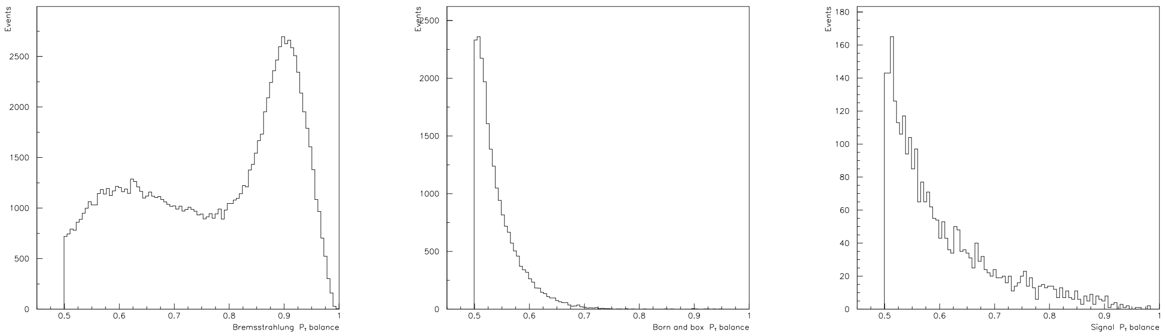

Bremsstrahlung Born, box Signal

Figure 7.6: The $P_T^{balance}$ cut parameter for the bremsstrahlung, Born plus box and the signal. The luminosities are 7 fb$^{-1}$ for the backgrounds, while 100 fb$^{-1}$ for the signal.

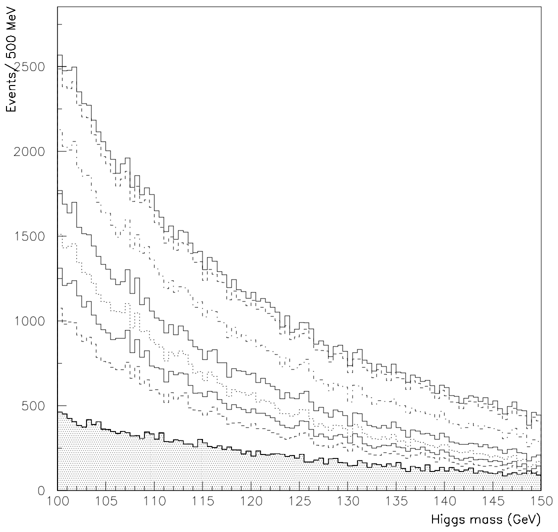

Figure 7.7: Reconstructed bremsstrahlung background for different values of the $P_T$ balance cut and the Born plus box background (shaded) at 7 fb$^{-1}$.

| $P_T^{balance}$ | **Bremsstrahlung**<br>% (events) | **Born, box**<br>% (events) | **Signal**<br>% (events) |
|---|---|---|---|
| No cut | (113219) | (21804) | (2854) |
| 0.95 | 95.3 (107925) | 100.0 (21801) | 99.9 (2850) |
| 0.90 | 77.2 (87357) | 99.9 (21788) | 99.0 (2826) |
| 0.85 | 59.7 (67610) | 99.9 (21777) | 97.2 (2774) |
| 0.80 | 49.9 (56515) | 99.8 (21769) | 94.0 (2684) |
| 0.75 | 42.3 (47940) | 99.8 (21755) | 89.2 (2545) |
| 0.70 | 34.5 (39063) | 99.4 (21681) | 83.7 (2388) |

Table 7.3: The impact of the bremsstrahlung background, Born and box and the signal from the $P_T^{balance}$ cut. The luminosities are 7 fb$^{-1}$ for the backgrounds, while 100 fb$^{-1}$ for the signal.

### 7.3.3 Reducible

The reducible QCD background requires full simulation to reconstruct. In order to delimit my thesis and to be able to finish in prescribed time I have not looked into this at all. I have only assumed what the TDR states; that this background amounts to about 40% of the irreducible background (Born, box and bremsstrahlung). I will use this in my later results.

### 7.3.4 Discussion

Apparently, it seems that the fast simulation software is not able to do a proper simulation of the bremsstrahlung process. With the hardest cut introduced to the bremsstrahlung, I managed to reduce it to roughly twice the size of Born plus box. But the achievement is useless, because of the large amount of signal events cut away as well.

Some ideas of why the fast simulation can not handle this is:

- The QED bremsstrahlung is only modelled with parton shower in PYTHIA and its rates are very uncertain;
- The photon isolation in PYTHIA/ATLFAST is based on very crude and loose criteria.

Two traditional approaches exist to model final-state radiation; the matrix element method and the parton shower method. In principle the matrix element method is the correct approach, which takes into account exact kinematics. It is in this way Feynman diagrams are calculated, order by order. The disadvantage is that the method can be difficult at higher order, and especially in loop diagrams. The second approach, with parton showers, is more an approximation. By simplifying the kinematics and using partons to yield a description of multi-jet events, the method is more flexible and usually the first choice. However, the shower approach has limited predictive power for the rate of well-separated jets. So for the bremsstrahlung process, the matrix element calculation should be used in order to obtain accurate results.

Due to the last point, I tried to introduce a photon isolation criterion in the analysis, but ended up no better than with the $P_T$ balance cut. With fast simulation, such studies would be very analysis dependent.

Since both the QCD and the bremsstrahlung backgrounds should be generated by other means (full simulation), it is hard for me to do a complete study of this channel. In order to evaluate the impact of a cut, one should have all the important processes to perform the cut on. That is why I sticked to the cuts used for the TDR, so I could be able to assume the two limits on the bremsstrahlung and QCD processes (the bremsstrahlung; $\sim 50\%$ of Born plus box, and the QCD; $\sim 40\%$ of the total irreducible background).

## 7.4 Statistical treatment of the data

Figure 7.8 shows signal and background for a Higgs mass of 120 GeV at four different luminosities. The background consists of the contribution from Born and box scaled up 2.1 times. With this scaling, the bremsstrahlung and QCD background are included;

$$N_{brems} = 0.5 * N_{Born,box}\ ,\ \ N_{reducible} = 0.4 * N_{irreducible},$$

giving a total background of

$$N_{total} = 1.4 * 1.5 * N_{Born,box} = 2.1 * N_{Born,box}.$$

The histograms are fitted with a combination of a Gaussian and a polynomial of third order. In the case of one year at high luminosity (100 fb$^{-1}$) (a), the signal is clearly visible above the background. The situation is worse for the lower luminosities. At 30 fb$^{-1}$ (b) one might be able to see the signal, while for 10 fb$^{-1}$ (d) the background fluctuation is so large it is hard (or even impossible) to extract the signal. Some of the peaks from the background fluctuation looks as much as a signal peak as the “true” signal.

The number of events generated for the signal and background for the different luminosities are listed in table 7.4. The numbers reflects the course of the cross-sections as shown in figure 7.1 and 7.3. The numbers are the ones used in PYTHIA for event generation, which means they only represents the unconverted photon events. For the analysis, the background is split into two ranges, 100-150 GeV and 120-170 GeV, where two signals are analysed in each range.

After splitting the events into two channels; (1) events with no photon conversions and (2) events with one or both photons converted, the signal and background histogram for 100 fb$^{-1}$ looks like in figure 7.9 (1) and (2). There are much fewer events in the case with converted photons, and at low luminosity this is a problem, because it is getting even harder to find the signal.

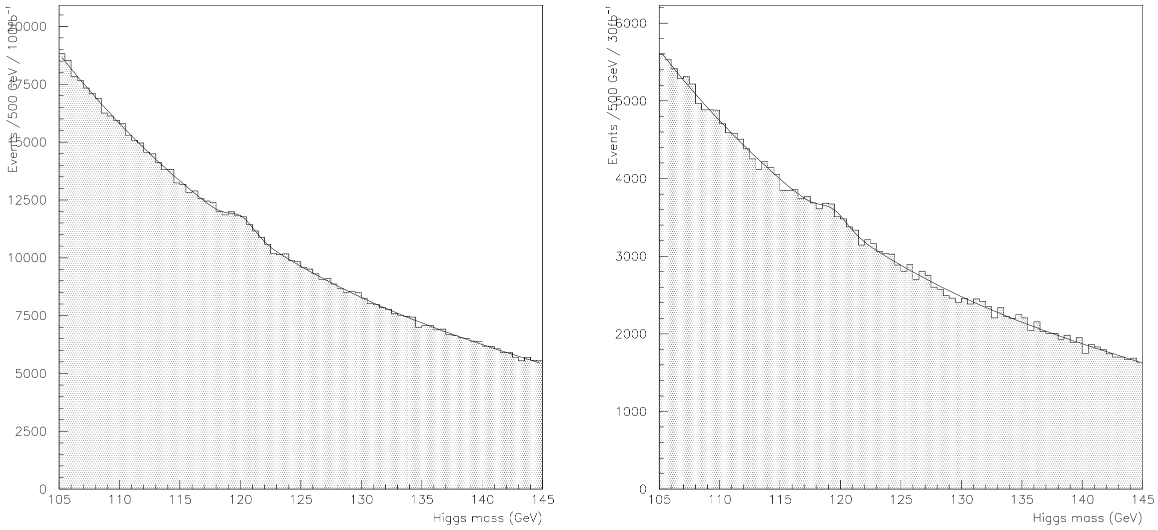

(a) 100 fb$^{-1}$ (b) 30 fb$^{-1}$

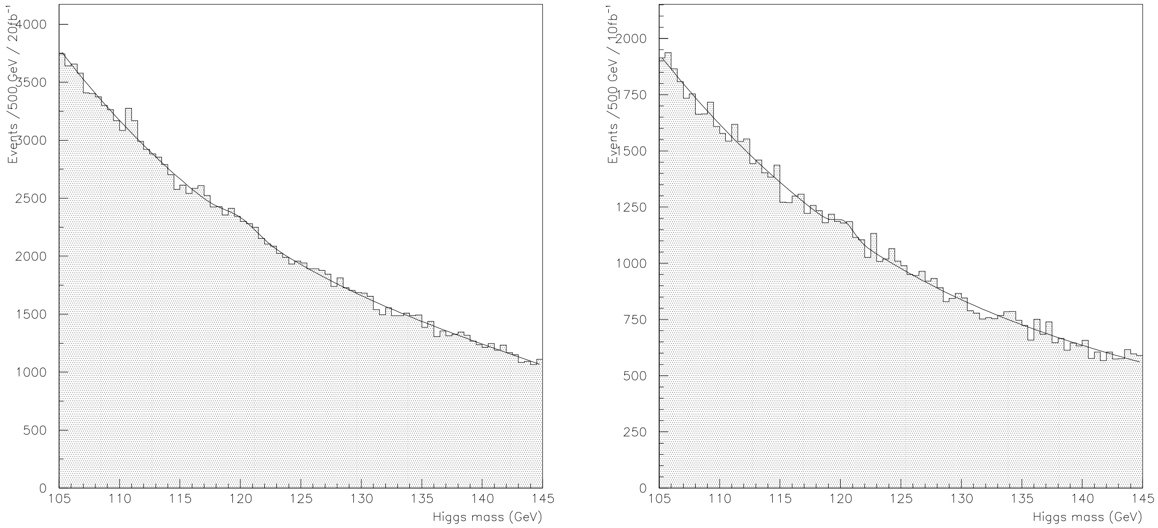

(c) 20 fb$^{-1}$ (d) 10 fb$^{-1}$

Figure 7.8: Signal and background for $H \to \gamma\gamma$ with a Higgs mass of 120 GeV at four different luminosities. The histograms are fitted with a combination of a Gaussian (for the signal) and a polynomial of third order.

| | 10 fb$^{-1}$ | 20 fb$^{-1}$ | 30 fb$^{-1}$ | 100 fb$^{-1}$ |
|---|---|---|---|---|
| Background 100-150 GeV | $3.95*10^5$ | $7.90*10^5$ | $1.18*10^6$ | $3.95*10^6$ |
| Signal at 120 GeV | 301 | 602 | 902 | 3008 |
| Signal at 130 GeV | 275 | 550 | 826 | 2752 |
| Background 120-170 GeV | $2.17*10^5$ | $4.35*10^5$ | $6.53*10^5$ | $2.17*10^5$ |
| Signal at 140 GeV | 224 | 447 | 671 | 2236 |
| Signal at 150 GeV | 150 | 300 | 450 | 1496 |

Table 7.4: The number of events generated for the analysis at different luminosities.

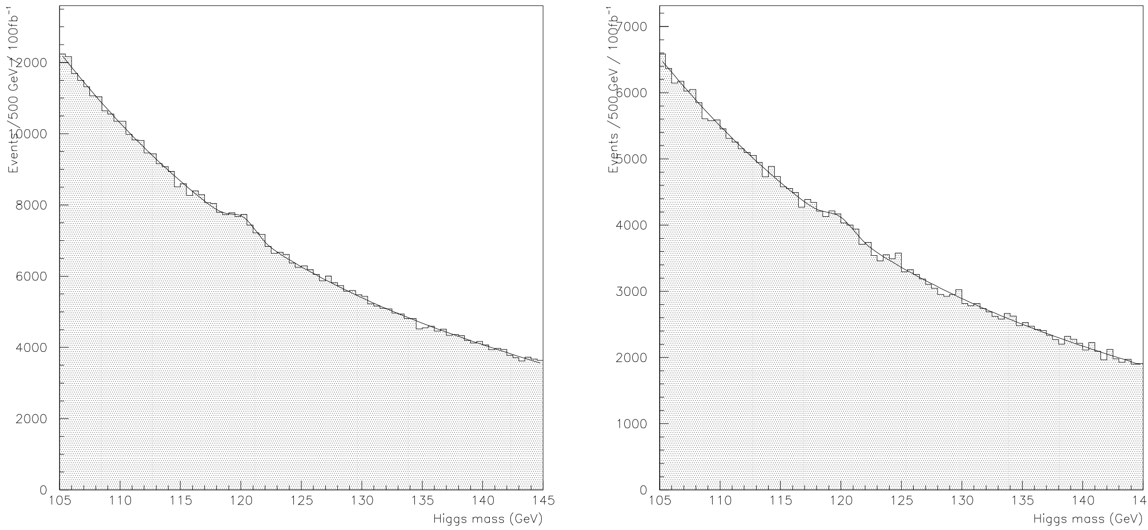

(1) Unconverted photons

(2) Converted photons

Figure 7.9: Signal and background for $H \rightarrow \gamma\gamma$ with a Higgs mass of 120 GeV at high luminosity. Histogram (1) is events without photon conversions and (2) is events with one or both photons converted. The histograms are fitted with a combination of a Gaussian (for the signal) and a polynomial of third order.

### 7.4.1 Significance found by using counting experiments

With the counting method, the significance is calculated as $S/\sqrt{B}$ in a given mass window. The mass window is a symmetrical interval around the mean value of the fitted Gaussian:

$$\mu \pm \sigma\xi \tag{7.3}$$

where $\sigma$ is the standard deviation of the fitted Gaussian (the signal). The only parameter that varies freely here is the window parameter $\xi$, and it has to be chosen in such a way that the significance is maximised. Figure 7.10 shows the variation of significance for different values of $\xi$. (The plot will surely look somewhat different for other masses and at other luminosities, but this is only to choose a value.) Based on this figure, the parameter is set to be $\xi = 2.0$ throughout the analysis.

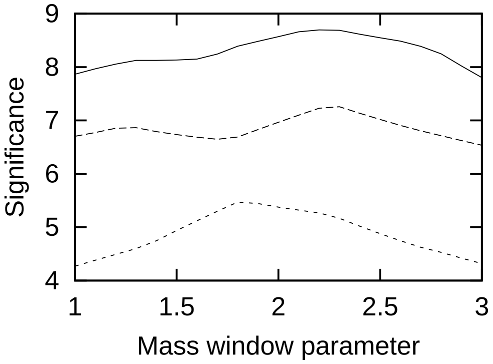

Figure 7.10: The significance for different mass window parameters for a Higgs mass of 120 GeV and at high luminosity. The dotted line is for events with one or more converted photon, the dashed for unconverted photon events and the line for all $\gamma\gamma$ events.

In figure 7.11, the counting significance is plotted for various luminosities and Higgs masses using both one and two channels. These results are achieved by the counting experiment explained in sections 5.1.1 and 5.2.1 and each point is the mean value of three independent experiments (runs). The plotted values are also in table 7.5. In appendix B, all the values from the three runs are listed.

The uncertainty in the significance, given with equation (5.3) is calculated for one measurement (120 GeV, high luminosity). The number of signal events as a result from the fitting is $S \pm \Delta S = 2614 \pm 372$ ($B \sim 92000$). This gives a uncertainty of the significance of $\Delta s = 1.2\sigma$. For other masses and luminosities this uncertainty is more or less the same. I tested the procedure on several other cases, and the uncertainty always ended up being one, or a little larger. This is logical, because when $S$ and $\Delta S$ decreases, the background decreases as well. With two channels, the uncertainties will have to be combined, and this gives an uncertainty which is a bit larger than with one channel, roughly around 1.5.

### 7.4.2 Significance found by using the $\chi^2$ method

A counting experiment is not always the optimum. A more advanced way to calculate the significance is by the $\chi^2$ method explained in sections 5.1.2 and 5.2.2. It takes into account a wider range of the histogram and not only the small mass window around the signal. In figure 7.12 the significance is plotted for four Higgs masses and four luminosities. Again, the mean value of three experiments is used. The plotted values can also be seen in table 7.6, and the values from the three runs in appendix B. The goodness of fit and the values for accepting the S+B hypothesis as explained in section 5.1.2 are added in super- and subscript in the table of run one in appendix B.

### 7.4.3 Discussion

The significance calculations in the two previous sections are based on exactly the same sets of data. That way, the obtained values reflects only the difference in the methods, and not the randomness in the histograms. Moreover, the histograms used are totally independent of each other.

From the figures 7.11 and 7.12 it is obvious that the significance from the chi-square method is higher than with the counting method. At high luminosity the difference is roughly one sigma, while at the lower luminosities the gain is more fluctuating, but less. In addition, using the chi-squares is a more optimal method than the counting because it treats the whole S+B histogram range, and not only where the signal is.

It is also obvious that the gain in significance by splitting the data into two data sets is significant. The gain for the high luminosity cases are in the range 0.1-0.8 sigma, typically 0.3 or 0.4. However, this is not clear for the lower luminosities. At one year with low luminosity the significance using one channel is often larger than with two (consult the tables 7.5 and 7.6). This is because the histograms with one or more converted photons have fewer events, and the analysis often failed to find the signal for the lowest luminosity. When this occurred, there were only contributions from one channel, and hence the significance is smaller.

The uncertainty in the calculation of the significance should only be taken as an indication of how much the significance can fluctuate. I will not go into a detailed study of the uncertainties of the significances, but with the calculation in the counting experiment simply express the magnitude which is somewhere between 1.0 and 1.5$\sigma$. The uncertainty in the mean of three runs can be expected to be less than one sigma.

The significances in the two tables and figures are the mean of three runs, but still they do fluctuate. This is due to the background fluctuation, and the relative background fluctuation is inverse proportional to the amount of events in the histogram. That means this relative fluctuation is largest for low luminosity and also for the highest Higgs masses. In table 7.4, where the amount of generated events are listed, this can be seen clearly. Some entries that differ are the small dip at the values for 140 GeV at 30 fb$^{-1}$ for both methods and some other entries. These deviations can be understood by having the uncertainty of the significance in mind.

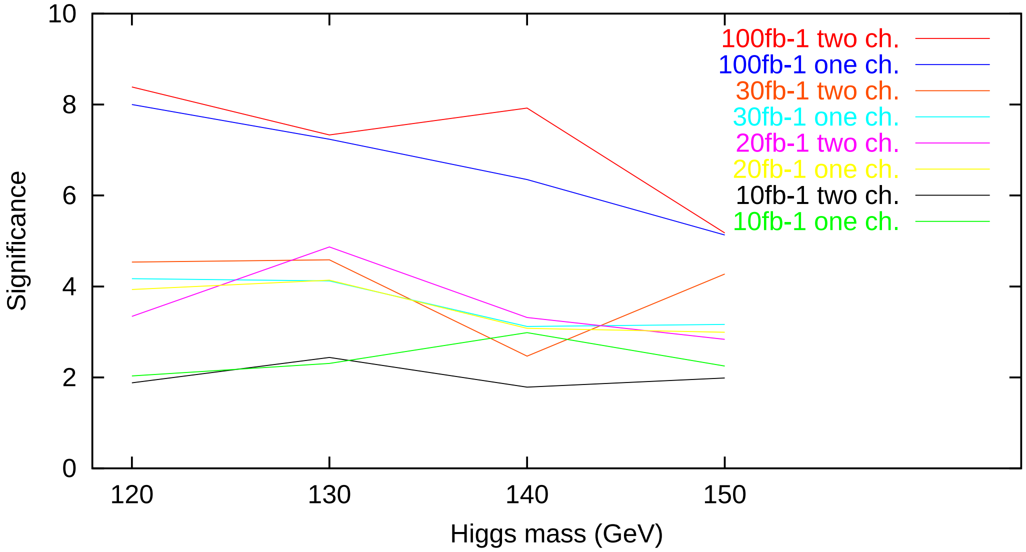

Figure 7.11: The significance from a counting experiment for different Higgs masses and at four luminosities. The plotted values are the mean from three independent runs.

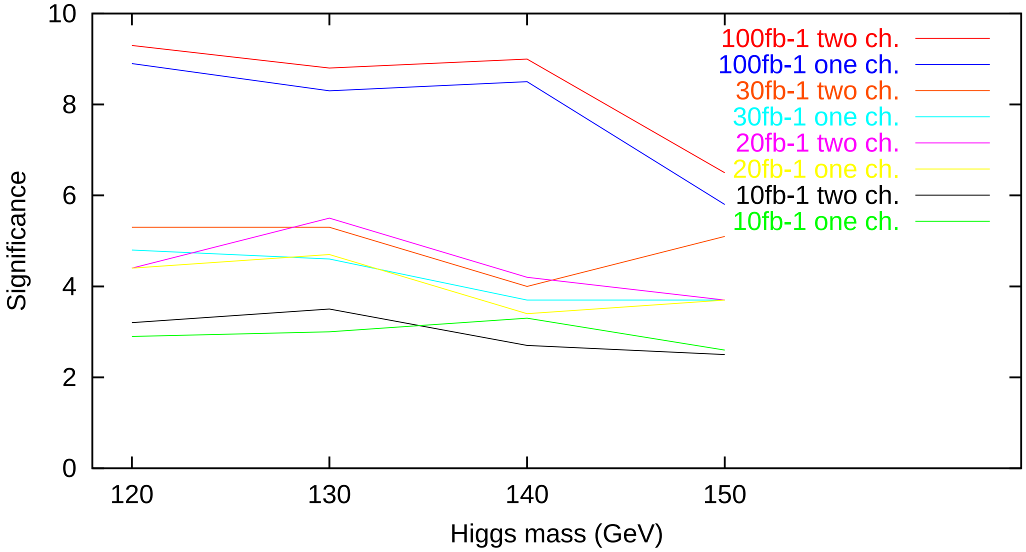

Figure 7.12: The significance from a statistical $\chi^2$ method for different Higgs masses and at four luminosities. The plotted values are the mean from three independent runs.

| **mH 120 GeV** | 10 fb$^{-1}$ | 20 fb$^{-1}$ | 30 fb$^{-1}$ | 100 fb$^{-1}$ |
|---|---|---|---|---|
| $signf._{two\ ch.}$ | 1.9 | 3.3 | 4.5 | 8.4 |
| $signf._{one\ ch.}$ | 2.0 | 3.9 | 4.2 | 8.0 |
| **mH 130 GeV** | | | | |
| $signf._{two\ ch.}$ | 2.4 | 4.9 | 4.6 | 7.3 |
| $signf._{one\ ch.}$ | 2.3 | 4.1 | 4.1 | 7.2 |
| **mH 140 GeV** | | | | |
| $signf._{two\ ch.}$ | 1.8 | 3.3 | 2.5 | 7.9 |
| $signf._{one\ ch.}$ | 3.0 | 3.1 | 3.1 | 6.4 |
| **mH 150 GeV** | | | | |
| $signf._{two\ ch.}$ | 2.0 | 2.8 | 4.3 | 5.2 |
| $signf._{one\ ch.}$ | 2.3 | 3.0 | 3.2 | 5.1 |

Table 7.5: Significance for the counting experiment, with both one and two channels at various luminosities. The values are the mean of three runs.

| **mH 120 GeV** | 10 fb$^{-1}$ | 20 fb$^{-1}$ | 30 fb$^{-1}$ | 100 fb$^{-1}$ |
|---|---|---|---|---|
| $signf._{two\ ch.}$ | 3.2 | 4.4 | 5.3 | 9.3 |
| $signf._{one\ ch.}$ | 2.9 | 4.4 | 4.8 | 8.9 |
| **mH 130 GeV** | | | | |
| $signf._{two\ ch.}$ | 3.5 | 5.5 | 5.3 | 8.8 |
| $signf._{one\ ch.}$ | 3.0 | 4.7 | 4.6 | 8.3 |
| **mH 140 GeV** | | | | |
| $signf._{two\ ch.}$ | 2.7 | 4.2 | 4.0 | 9.0 |
| $signf._{one\ ch.}$ | 3.3 | 3.4 | 3.7 | 8.5 |
| **mH 150 GeV** | | | | |
| $signf._{two\ ch.}$ | 2.5 | 3.7 | 5.1 | 6.5 |
| $signf._{one\ ch.}$ | 2.6 | 3.7 | 3.7 | 5.8 |

Table 7.6: Significance for the chi-square method experiment, with both one and two channels at various luminosities. The values are the mean of three runs.

To claim discovery of a particle, the significance should be larger than five sigmas (the famous five sigma rule). The entries that has a significance larger than five are: all at 100 $\text{fb}^{-1}$ and some at 30 $\text{fb}^{-1}$. The entries for the masses 120, 130 and 150 GeV at 30 $\text{fb}^{-1}$ are barely above the limit, but due to uncertainties they *may* be just under the limit when running the LHC (or higher, who knows).

The size of the background in this channel is very uncertain. It should be in this order of magnitude, but can be expected to differ. Especially the rates of the bremsstrahlung and the QCD background are uncertain, and they should be looked further up on, using full simulation. Both the methods have a significance which goes as $1/\sqrt{B}$. In the counting method, this is explicit while in the chi-square method the $\chi^2$ goes as $1/\sigma^2$ where $\sigma^2 \sim N_B$ (Poisson statistics) and the significance is the square-root of the $\Delta\chi^2$. This means that a doubling in the background results in a $\sim 70\%$ lower significance ($1/\sqrt{2}$). Still the Higgs can be observed (the significance is higher than five) for the masses 120, 130 and 140 GeV at high luminosity.

Let's try to put a $\text{fb}^{-1}$-tag on the performance using two channels and the chi-square method. Generalising the results, the gain in using two channels and the chi-square method instead of one channel and counting is roughly $1.5\sigma$ at 100 $\text{fb}^{-1}$ and $1.0\sigma$ at 30 $\text{fb}^{-1}$. If one manipulates these numbers, and in addition looks at the progress of the significance in the tables, the gain in $\text{fb}^{-1}$ after three years would be something like 10 $\text{fb}^{-1}$ and after four years, 30 $\text{fb}^{-1}$. Of course, this is only an estimate, and only of $H \to \gamma\gamma$ at ATLAS. There is a well known fact that *time is money* [34], and this means that the gain in $\text{fb}^{-1}$ would correspond to a lot of money (but the analogy to money is really a bit doubtful, because at the LHC, there are many other projects, not only regarded Higgs search).

In the analysis done for the TDR [2], the counting method is used to calculate the significance of the signal. It ended up with a significance of $6.5\sigma$ at 100 $\text{fb}^{-1}$ ($4.0\sigma$ at 30 $\text{fb}^{-1}$) for the Higgs masses 120 and 130 GeV. In this analysis, the associated Higgs production (<100 signal candidates) is included, and a mass window of $\pm 1.4\sigma$ around the nominal Higgs mass is chosen. My results, using one channel and counting, is $1.5\sigma$ higher than these results. Some of the difference may lie in the choice of mass window. When I tried to use the same mass interval as the TDR, the significance was reduced some (but not as much as $1.5\sigma$). Another thing to notice is that I have done the calculation for three sets of data, which makes the results more stable than just doing it once. In addition to this, the algorithms used in the methods may be somewhat different, and certainly uncertainties in the significance must be considered.

For future study of this channel, it might be possible to use the program ALRMC (C++) (introduced in section 5.4). With this method, the discovery potential will be thoroughly examined. Some of my data was fed into a very preliminary version of the new program, and an output in the form of a counting significance, was in accordance with my results. It was tested for 120 GeV, high luminosity, one channel, and the significance was about $\sim 9\sigma$ with the worst and best estimate of 7 and 14 $\sigma$ (the significance may lay in this interval). But again, this is only a test of the program, and should not be taken as an absolute result.

## 7.5 Reconstructed Higgs mass

In the simulations, the signal is generated at a certain mass. The signal is then placed onto the background, and afterwards fitted with a Gaussian. The question is whether one ends up with a Higgs mass corresponding to the value inserted in the simulations at the beginning.

Table 7.7 shows all the reconstructed Higgs masses at the four luminosities, with uncertainties. The uncertainties are output from PAW regarding the fitting procedure. There are some small deviations from the nominal Higgs mass, and especially at the low luminosities. Mainly one value is very off, and that is the reconstructed mass of 133.89±0.20 GeV for the 130 GeV Higgs. This is when using two channels at 30 fb$^{-1}$. What happened here is that the channel with converted photons found a signal (well, actually it is background fluctuation) at 134.50±0.22 GeV with a significance of only $1\sigma$ (counting). The channel with unconverted photons fitted the signal at 130.83±0.49 GeV, so this is ok.

The reconstructed standard deviations of the fitted Gaussians does also vary from the values they should have had after the event generation. This is because a fit is performed, and fluctuation in the background is very interfering since the amount of signal events is small compared to the background events. A few bins with extra events (or less) on the wing of the signal in the S+B histogram will mean a larger (smaller) standard deviation for the fitted Gaussian.

| **mH 120 GeV** | 10 fb$^{-1}$ | 20 fb$^{-1}$ | 30 fb$^{-1}$ | 100 fb$^{-1}$ |
|---|---|---|---|---|
| $mH_{two\ ch.}$ | 120.32 ±0.16 | 120.18 ±0.55 | 119.25 ±0.26 | 120.18 ±0.15 |
| $mH_{one\ ch.}$ | 120.37 ±0.44 | 120.06 ±0.65 | 119.46 ±0.33 | 120.18 ±0.15 |
| **mH 130 GeV** | | | | |
| $mH_{two\ ch.}$ | 130.05 ±0.17 | 129.18 ±0.46 | 133.89 ±0.20 | 129.66 ±0.10 |
| $mH_{one\ ch.}$ | 129.88 ±0.25 | 129.01 ±0.61 | 131.16 ±0.39 | 129.78 ±0.19 |
| **mH 140 GeV** | | | | |
| $mH_{two\ ch.}$ | 140.81 ±0.71 | 139.02 ±0.41 | 138.16 ±0.23 | 139.78 ±0.21 |
| $mH_{one\ ch.}$ | 140.24 ±2.29 | 139.18 ±0.47 | 138.67 ±1.19 | 139.93 ±0.17 |
| **mH 150 GeV** | | | | |
| $mH_{two\ ch.}$ | 148.95 ±0.90 | 149.59 ±0.13 | 149.83 ±0.33 | 149.77 ±0.22 |
| $mH_{one\ ch.}$ | 149.12 ±1.42 | 149.69 ±0.18 | 149.66 ±0.41 | 149.74 ±0.26 |

Table 7.7: Reconstructed Higgs mass for run one.

# Chapter 8

# Conclusion and Outlook

An analysis of the channel $H \to \gamma\gamma$ has been performed using fast simulation tools. The signal and background are presented, and the background seems to be under full control. However, the rates of the bremsstrahlung process and the QCD background could need an update. This is out of the scope for this master thesis, since it requires full simulation.

The outcome of the significance calculation is very promising, and gives a better result than the analysis done for the ATLAS Technical Design Report [2]. There is a gain in the significance both by using the chi-square statistical method instead of the ordinary counting method, and by splitting the events into two channels (with different signal resolution).

So, if there exists a Higgs boson in the mass region 120 - 150 GeV, it can (most probable) be discovered after four years at the LHC using only the $H \to \gamma\gamma$ channel. Using my methods, it may even be discovered after three years.

For future studies of this and other channels the program ALRMC may be an important tool in the search for the Higgs boson, and in addition, one should be aware of the radion, which has similar characteristics.

With the runs of the Tevatron (at Fermilab) and LHC, we should be able to discover or exclude the Standard Model Higgs boson at *any* mass. Whether the Higgs boson is the solution to the mass mystery originating from Peter Higgs in the 60s, only the future can tell.

# Appendix A

# Simulation parameters

This appendix contains comments about some of the most important parameters used for my analysis with PYTHIA and ATLFAST. To be able to read this information the reader should be acquainted with the simulation software and its technicalities. For further information consult the manuals [20] and [21].

### PYTHIA and ATLFAST

- I have been using PYTHIA 6.152 and ATLFAST 2.51 and the standard setup with the file demo.f.
- In `demo.f`:
  - Select the signal processes by choosing MSEL=16 which gives the processes ISUB=3,102,103[1],123,124, and the background processes with ISUB=18 (Born), ISUB=114 (box), ISUB=14,29,115 (bremsstrahlung).
  - CKIN(1), CKIN(2) defines a lower and upper limit on the centre of mass energy. This is very useful when generating the signal and the Born and box backgrounds, because the events will only be in this two-photon mass range. However, for the bremsstrahlung process, the CKINs is not a limit on the two-photon invariant mass alone. This is because the final state consists of not only two photons, but an extra particle. So for the bremsstrahlung process, only CKIN(1) should be used to reduce *some* of the events below the two-photon mass limit.
- In `atlfast.dat`:
  - $\eta$ coverage for photons, YPAR(31),TPAR( 9,1)=2.400
  - $P_T$ triggering for photons, TPAR( 2,1),TPAR( 2,2)=40.0
    and TPAR( 3,1),TPAR( 3,2)=25.0

---

[1] This process ($\gamma\gamma \rightarrow H$) had a vanishing cross-section in PYTHIA and was switched off.

- In addition, I made some of my cuts directly in the file `atlfastntup.F`, but it is a matter of taste of doing them here or directly in PAW. In general it is best to do as few cuts as possible when generating the events, but it can be important in order to reduce the size of the ntuple.
- The output comes as a ntuple and a text file `demo.out`. This latter file contains the cross-sections for the processes in addition to other information.

### Parallel Computing

These are the changes I had to do in order to run with MPI. In addition, the program have to be compiled with a MPI compiler and also run with a MPI program.

- Add these lines after the declarations in `demo.f`:

  ```
  CALL MPI_INIT(IERR)
  CALL MPI_COMM_SIZE(MPI_COMM_WORLD,size,IERR)
  CALL MPI_COMM_RANK(MPI_COMM_WORLD,my_rank,IERR)
  CALL MPI_GET_PROCESSOR_NAME(processor_name,namelen,IERR)
  print *,"Process ",my_rank, processor_name}
  ```

- To split the events between the machines, type

  ```
  DO II= 1, NPAR(10)/SIZE
  ```

  instead of

  ```
  DO II= 1,NPAR(10)
  ```

  (in the loop over events which calls PYTHIA and ATLFAST).

- Add

  ```
  CALL MPI_FINALIZE(IERR)
  ```

  before `END` in the main program.

- Also, change the code to write a ntuple- and an outfile for each machine, and make sure each machine gets an unique seed to the random generator.
  I solved this problem by adding the rank of the machine to the seed:

  ```
  NPAR(12)=NPAR(12)+MY_RANK
  ```

  All the machines have a different rank and with this method the machines will get different random numbers.

# Appendix B

# Significances for the three runs

In this appendix all the values from the three runs used to find the significances for the counting and chi-square methods are listed in tables. The experiments are described in section 7.4 where only the mean values of the three runs are presented.

### Notation and comments about the following tables

- The histograms used for the two methods in each run are the same, but the three runs are independent.
- $\Delta\chi^2_{unco}$ and $\Delta\chi^2_{co}$ are the delta chi-squares for the two separate channels, events with **unco**nverted photons and events with at least one **co**nverted photon.
- The super- and subscript in the chi-square table in (only) run one, are the quantities $\chi^2_{S+B}/d.o.f.$ and $\chi^2_B/d.o.f.$ which represents the goodness of fit and the S+B hypothesis testing (consult section 5.1.2).
- The fields containing a $*$ are cases where the method has failed to find the signal. This is mostly due to too little statistics, and/or background fluctuation, thus, it happens most often in the converted channels and in the low luminosity/high mass corner of the tables.

## RUN 1
## COUNTING

| **mH 120 GeV** | 10 fb$^{-1}$ | 20 fb$^{-1}$ | 30 fb$^{-1}$ | 100 fb$^{-1}$ |
|---|---|---|---|---|
| $signf._{two\ ch.}$ | 1.2 | 2.8 | 4.9 | 8.8 |
| $signf._{one\ ch.}$ | 2.0 | 3.5 | 4.7 | 8.6 |
| **mH 130 GeV** | | | | |
| $signf._{two\ ch.}$ | 1.6 | 4.9 | 3.1 | 8.0 |
| $signf._{one\ ch.}$ | 1.4 | 4.8 | 2.7 | 7.8 |
| **mH 140 GeV** | | | | |
| $signf._{two\ ch.}$ | 1.8 | 2.8 | 2.9 | 7.8 |
| $signf._{one\ ch.}$ | 2.4 | 2.8 | 3.1 | 6.6 |
| **mH 150 GeV** | | | | |
| $signf._{two\ ch.}$ | 2.5 | 1.0 | 4.4 | 6.1 |
| $signf._{one\ ch.}$ | 1.7 | 0.6 | 4.3 | 5.6 |

## CHISQUARE METHOD

| **mH 120 GeV** | 10 fb$^{-1}$ | 20 fb$^{-1}$ | 30 fb$^{-1}$ | 100 fb$^{-1}$ |
|---|---|---|---|---|
| $\Delta\chi^2_{unco}$ | $4.8^{1.1}_{1.2}$ | $3.6^{1.0}_{1.1}$ | $23.4^{1.0}_{1.3}$ | $65.5^{1.0}_{1.9}$ |
| $\Delta\chi^2_{co}$ | $4.3^{1.3}_{1.4}$ | $7.9^{0.9}_{1.0}$ | $15.2^{1.1}_{1.3}$ | $32.9^{1.2}_{1.7}$ |
| $signf._{two\ ch.}$ | 3.0 | 3.4 | 6.2 | 9.9 |
| $signf._{one\ ch.}$ | $2.5^{1.2}_{1.3}$ | $3.5^{1.0}_{1.2}$ | $5.4^{1.1}_{1.5}$ | $9.7^{1.0}_{2.2}$ |
| **mH 130 GeV** | | | | |
| $\Delta\chi^2_{unco}$ | $7.0^{1.0}_{1.1}$ | $16.6^{1.0}_{1.2}$ | $10.2^{1.0}_{1.1}$ | $75.7^{1.0}_{2.0}$ |
| $\Delta\chi^2_{co}$ | $2.4^{1.3}_{1.3}$ | $8.5^{0.8}_{1.0}$ | $6.5^{1.1}_{1.2}$ | $22.4^{1.1}_{1.4}$ |
| $signf._{two\ ch.}$ | 3.1 | 5.0 | 4.1 | 9.9 |
| $signf._{one\ ch.}$ | $2.4^{1.2}_{1.2}$ | $5.0^{1.0}_{1.3}$ | $3.0^{1.0}_{1.1}$ | $8.7^{1.0}_{2.0}$ |
| **mH 140 GeV** | | | | |
| $\Delta\chi^2_{unco}$ | $6.5^{0.8}_{0.9}$ | $12.6^{1.4}_{1.6}$ | $11.2^{1.4}_{1.5}$ | $54.0^{0.8}_{1.6}$ |
| $\Delta\chi^2_{co}$ | * | $1.7^{1.1}_{1.2}$ | $2.6^{1.0}_{1.0}$ | $19.0^{0.9}_{1.2}$ |
| $signf._{two\ ch.}$ | 2.6 | 3.8 | 3.7 | 8.5 |
| $signf._{one\ ch.}$ | $3.1^{0.6}_{0.8}$ | $3.0^{1.3}_{1.4}$ | $3.4^{1.4}_{1.5}$ | $8.0^{0.9}_{1.8}$ |
| **mH 150 GeV** | | | | |
| $\Delta\chi^2_{unco}$ | $9.7^{0.8}_{1.0}$ | $10.8^{1.4}_{1.5}$ | $14.3^{1.4}_{1.6}$ | $50.9^{0.8}_{1.5}$ |
| $\Delta\chi^2_{co}$ | * | * | $14.2^{1.0}_{1.2}$ | $2.0^{0.9}_{0.9}$ |
| $signf._{two\ ch.}$ | 3.1 | 3.3 | 5.3 | 7.3 |
| $signf._{one\ ch.}$ | $1.8^{0.7}_{0.7}$ | $2.0^{1.3}_{1.3}$ | $4.5^{1.4}_{1.7}$ | $6.4^{0.8}_{1.4}$ |

Table B.1: The significances from run one, using the counting experiment (top table) and the chi-square method (bottom table) for four Higgs masses and four luminosities. The notation is explained on page 57.

## RUN 2

## COUNTING

| **mH 120 GeV** | 10 $\mathrm{fb}^{-1}$ | 20 $\mathrm{fb}^{-1}$ | 30 $\mathrm{fb}^{-1}$ | 100 $\mathrm{fb}^{-1}$ |
|---|---|---|---|---|
| $signf._{two\ ch.}$ | 2.2 | 3.2 | 3.3 | 9.0 |
| $signf._{one\ ch.}$ | 2.6 | 3.8 | 2.6 | 8.1 |
| **mH 130 GeV** | | | | |
| $signf._{two\ ch.}$ | 3.2 | 5.7 | 5.1 | 6.0 |
| $signf._{one\ ch.}$ | 3.5 | 4.7 | 4.4 | 5.8 |
| **mH 140 GeV** | | | | |
| $signf._{two\ ch.}$ | 2.3 | 3.4 | 1.9 | 6.9 |
| $signf._{one\ ch.}$ | 3.3 | 3.2 | 2.4 | 5.2 |
| **mH 150 GeV** | | | | |
| $signf._{two\ ch.}$ | 2.2 | 5.2 | 4.5 | 4.4 |
| $signf._{one\ ch.}$ | 2.3 | 4.7 | 3.2 | 4.5 |

## CHISQUARE METHOD

| **mH 120 GeV** | 10 $\mathrm{fb}^{-1}$ | 20 $\mathrm{fb}^{-1}$ | 30 $\mathrm{fb}^{-1}$ | 100 $\mathrm{fb}^{-1}$ |
|---|---|---|---|---|
| $\Delta\chi^2_{unco}$ | 14.6 | 12.5 | 7.4 | 72.9 |
| $\Delta\chi^2_{co}$ | * | 9.2 | 6.1 | 20.7 |
| $signf._{two\ ch.}$ | 3.8 | 4.7 | 3.7 | 9.7 |
| $signf._{one\ ch.}$ | 3.4 | 4.6 | 3.0 | 9.1 |
| **mH 130 GeV** | | | | |
| $\Delta\chi^2_{unco}$ | 11.3 | 14.2 | 17.4 | 29.3 |
| $\Delta\chi^2_{co}$ | * | 25.7 | 11.1 | 19.5 |
| $signf._{two\ ch.}$ | 3.4 | 6.3 | 5.3 | 7.0 |
| $signf._{one\ ch.}$ | 3.6 | 5.3 | 5.1 | 7.0 |
| **mH 140 GeV** | | | | |
| $\Delta\chi^2_{unco}$ | 8.1 | 5.1 | 8.6 | 42.6 |
| $\Delta\chi^2_{co}$ | * | 16.4 | 1.5 | 28.7 |
| $signf._{two\ ch.}$ | 2.8 | 4.6 | 3.2 | 8.4 |
| $signf._{one\ ch.}$ | 3.9 | 4.0 | 3.0 | 7.9 |
| **mH 150 GeV** | | | | |
| $\Delta\chi^2_{unco}$ | * | 30.4 | 12.8 | 28.2 |
| $\Delta\chi^2_{co}$ | 7.7 | * | 17.6 | 6.5 |
| $signf._{two\ ch.}$ | 2.8 | 5.5 | 5.5 | 5.9 |
| $signf._{one\ ch.}$ | 2.5 | 5.0 | 3.6 | 5.6 |

Table B.2: The significances from run two, using the counting experiment (top table) and the chi-square method (bottom table) for four Higgs masses and four luminosities. The notation is explained on page 57.

## RUN 3
## COUNTING

| **mH 120 GeV** | 10 $fb^{-1}$ | 20 $fb^{-1}$ | 30 $fb^{-1}$ | 100 $fb^{-1}$ |
|---|---|---|---|---|
| $signf_{\cdot two\ ch.}$ | 2.2 | 4.0 | 5.4 | 7.3 |
| $signf_{\cdot one\ ch.}$ | 1.5 | 4.7 | 5.2 | 7.3 |
| **mH 130 GeV** | | | | |
| $signf_{\cdot two\ ch.}$ | 2.5 | 4.1 | 5.6 | 8.0 |
| $signf_{\cdot one\ ch.}$ | 2.1 | 2.9 | 5.2 | 8.1 |
| **mH 140 GeV** | | | | |
| $signf_{\cdot two\ ch.}$ | 1.2 | 3.8 | 2.6 | 9.1 |
| $signf_{\cdot one\ ch.}$ | 3.2 | 3.3 | 3.8 | 7.3 |
| **mH 150 GeV** | | | | |
| $signf_{\cdot two\ ch.}$ | 1.3 | 2.3 | 3.9 | 5.0 |
| $signf_{\cdot one\ ch.}$ | 2.7 | 3.6 | 2.0 | 5.3 |

## CHISQUARE METHOD

| **mH 120 GeV** | 10 $fb^{-1}$ | 20 $fb^{-1}$ | 30 $fb^{-1}$ | 100 $fb^{-1}$ |
|---|---|---|---|---|
| $\Delta\chi^2_{unco}$ | 7.2 | 14.0 | 24.1 | 44.1 |
| $\Delta\chi^2_{co}$ | * | 11.4 | 12.4 | 24.2 |
| $signf_{\cdot two\ ch.}$ | 2.7 | 5.0 | 6.0 | 8.3 |
| $signf_{\cdot one\ ch.}$ | 2.8 | 5.2 | 5.9 | 8.0 |
| **mH 130 GeV** | | | | |
| $\Delta\chi^2_{unco}$ | 12.6 | 17.1 | 27.8 | 43.0 |
| $\Delta\chi^2_{co}$ | 4.7 | 8.8 | 15.2 | 46.6 |
| $signf_{\cdot two\ ch.}$ | 4.1 | 5.1 | 6.5 | 9.5 |
| $signf_{\cdot one\ ch.}$ | 3.2 | 3.9 | 5.8 | 9.2 |
| **mH 140 GeV** | | | | |
| $\Delta\chi^2_{unco}$ | 6.5 | 16.8 | 12.4 | 71.0 |
| $\Delta\chi^2_{co}$ | * | * | 12.4 | 29.4 |
| $signf_{\cdot two\ ch.}$ | 2.6 | 4.1 | 5.0 | 10.0 |
| $signf_{\cdot one\ ch.}$ | 3.7 | 3.3 | 4.6 | 10.5 |
| **mH 150 GeV** | | | | |
| $\Delta\chi^2_{unco}$ | 2.9 | 5.5 | 13.7 | 27.2 |
| $\Delta\chi^2_{co}$ | * | * | 7.2 | 12.3 |
| $signf_{\cdot two\ ch.}$ | 1.7 | 2.4 | 4.6 | 6.3 |
| $signf_{\cdot one\ ch.}$ | 3.2 | 4.2 | 3.0 | 5.5 |

Table B.3: The significances from run three, using the counting experiment (top table) and the chi-square method (bottom table) for four Higgs masses and four luminosities. The notation is explained on page 57.

# Bibliography

[1] CERN, *The Higgs Boson*, [online] May 2. 2002
`http://www.exploratorium.edu/origins/cern/ideas/higgs.html`

[2] ATLAS Collaboration, Detector and Physics Performance Technical Design Report, Vol. 2, CERN/LHCC/99-15 (1999)

[3] CERN, *CERN in 2 minutes*, [online] May 2. 2002
`http://public.web.cern.ch/Public/whatiscern.html`

[4] F. Gianotti, *Collider Physics: LHC*, Lectures given at the European School of High-Energy Physics, Casta Papiernicka, September 1999, ATL-CONF-2000-001

[5] CERN, *LHC - Challenges in Accelerator Physics*, [online] May 2. 2002
`http://press.web.cern.ch/lhc/general/acphys.htm`

[6] ATLAS Collaboration, ATLAS Technical Proposal, CERN/LHCC/94-43 (1994)

[7] CMS Collaboration, CMS Technical Proposal, CERN/LHCC/94-38 (1994)

[8] ALICE Collaboration, ALICE Technical Proposal, CERN/LHCC/95-71 (1995)

[9] LHCb Collaboration, LHCb Technical Proposal, CERN/LHCC/98-4 (1998)

[10] ATLAS Collaboration, Detector and Physics Performance Technical Design Report, Vol. 1, CERN/LHCC/99-14 (1999)

[11] W. R. Leo, *Techniques for Nuclear and Particle Physics Experiments*, Springer-Verlag, 2nd ed., ISBN: 0-387-57280-5 (1994)

[12] Centre de Physique des Particules de Marseille, *Electromagnetic End-Cap mechanics design*, [online] May 2. 2002
`http://marpix1.in2p3.fr/calo/intro.html`

[13] ATLAS Collaboration, First-Level Trigger Technical Design Report, CERN/LHCC/98-14 (1998)

ATLAS Collaboration, Trigger Performance Status Report, CERN/LHCC/98-15 (1998)

ATLAS Collaboration, DAQ, EF, LVL2 and DCS Technical Progress Report, CERN/LHCC/98-16 (1998)

[14] ATLAS Collaboration, Computing Technical Proposal, CERN/LHCC/96-43 (1996)

[15] B. R. Martin and G. Shaw, *Particle Physics*, John Wiley & Sons, Inc , 2nd ed., ISBN: 0-471-97285-1 (1997)

[16] The Super-Kamiokande Collaboration, *Evidence for massive neutrinos found*, [online] May 2. 2002
`http://www.ps.uci.edu/∼superk/announce.html`

The Super-Kamiokande Collaboration, Phys. Rev. Lett. **81** (1998), 1562

[17] F. Halzen and A. Martin, *Quarks and Leptons*, John Wiley & Sons, Inc, ISBN: 0-471-88741-2 (1984)

[18] P. W. Higgs, Phys. Lett. **12** (1964), 132

P. W. Higgs, Phys. Rev. Lett. **13** (1964), 508

P. W. Higgs, Phys. Rev. **145** (1966), 1156

F. Englert and R. Brout, Phys. Rev. Lett. **13** (1964) 321

[19] Tom Kibble, *Of Particles, Pencils and Unification*, [online] May 2. 2002
`http://www.phy.uct.ac.za/courses/phy400w/particle/higgs4.htm`

[20] T. Sjöstrand, Computer Physics Commun. **82** (1994), 74

T.Sjöstrand, Pythia 5.7 and Jetset 7.4 Physics and Manual, CERN-TH.7112/93 (1993)

[21] E. Richter-Was, D. Froidevaux and L. Poggioli, ATLAS Internal Note, ATL-PHYS-98-131 (1998)

[22] Argonne National Laboratory, *The Message Passing Interface (MPI) standard*, [online] May 2. 2002
`http://www-unix.mcs.anl.gov/mpi/`

[23] CERN computer center, *The PAW manual*, CERN Program Library Entry **Q121** (1989)

[24] A. L. Read, CERN Yellow Report 2000-005 (2000), 81

[25] A. L. Read, *Modified frequentist analysis of search results (the $CL_s$ method)*, in F. James, L. Lyons and Y. Perrin (eds.), Workshop on Confidence Limits, CERN Yellow Report 2000-005 (2000)

A. L. Read, DELPHI Collaboration Note 97-158 PHYS 737 (1997)

[26] A. L. Borg, Master thesis in experimentally particle physics at the University of Oslo, NB: Available after August 2002.

[27] A. Sopczak, hep-ph/0112082 (2001)

[28] J. F. Gunion, H. E. Haber, G. Kane and S. Dawson, *The Higgs Hunter's Guide*, Perseus publishing, First paperback ed., ISBN: 0-7382-0305-X (2000)

[29] D. Costanzo, ATL-CONF-2001-002 (2001)

E. Richter-Was, D. Froidevaux, F. Gianotti, L. Poggioli, D. Cavalli and L. Cozzi, ATLAS Internal Note, PHYS-NO-048 (1995)

V. Tisserand, ATLAS Internal Note, PHYS-NO-90 (1996)

[30] C. Roda,ATL-COM-PHYS-2002-016 (2002)

[31] L. Fayard, G. Unal, EAGLE Internal Note, PHYSICS-NO-001 (1992)

V. V. Zmushko, EAGLE Internal Note, PHYSICS-NO-002 (1992)

P. Aurenche, M. Bonesini, L. Camilleri, M. Fontannaz and M. Werlen, Proceedings of LHC Aachen Workshop CERN-90-10 G. Jarlskog and D. Rein eds., vol. II (1990), 83

[32] P. Osland, Talk given at the Lund Nordic LHC meeting March 2000, [online] available from:
`http://www.quark.lu.se/nordic-lhc/posland/`

P. Osland, Talk given at the Copenhagen Nordic LHC meeting Sept. 2000, [online] available from:
`http://alf.nbi.dk/HEP/nordic-lhc/slides/`

[33] L. Randall and R. Sundrum, Phys. Rev. Lett. **83** (1999), 3370

L. Randall and R. Sundrum, Phys. Rev. Lett. **83** (1999), 4690

[34] CNN, *SCI-TECH, Time is money, professor proves*, [online] May 29. 2002
`http://europe.cnn.com/2002/TECH/science/05/29/time.money/index.html`